SIGMA DELTA MODULATORS WITH HEXAGONAL QUANTIZATION

by

Glen Luckjiff

A dissertation submitted in partial fulfillment of
the requirements for the degree of

Doctor of Philosophy

(Electrical Engineering)

at the

UNIVERSITY OF WISCONSIN–MADISON

2003

UMI Number: 3089695

ProQuest Information and Learning Company
300 North Zeeb Road
P.O. Box 1346
Ann Arbor, MI 48106-1346

A dissertation entitled

Sigma Delta Modulators with Hexagonal Quantization

submitted to the Graduate School of the
University of Wisconsin-Madison
in partial fulfillment of the requirements for the
degree of Doctor of Philosophy

by

Glen Andrew Luckjiff

Date of Final Oral Examination: 12/23/2002

Month & Year Degree to be awarded: **December** **May** **August**

****

Approval Signatures of Dissertation Committee

Signature, Dean of Graduate School

Martin Cadwallader /EH

Committee's Page. This page is not to be hand-written except for the signatures

To my lovely wife Samantha.

ACKNOWLEDGMENTS

I would like to thank collegues at SoftSwitching Technologies and the University of Wisconsin - Madison including John Wohlbier, Ian Wallace, Giri Venkataramanan, Mukul Chandorkar, Ashish Bendre, Randy Gascoigne, and Steven Norris for many hours of brain storming and painstaking work that has brought the technology discussed in this dissertation to market.

I am indebted to the founder of SoftSwitching Technologies, Deepak Divan for his direction and generous support throughout my stay in Madison. His genuine zest for entrepreneurship and creativity have given me a true learning experience that shall be remembered.

I am deeply grateful to my advisor and friend Ian Dobson for his thoughtful conversation, patience, and generous support during the course of writing this dissertation. His extraordinary capabilities and keen sense of humor have and will always be a source of inspiration.

Special thanks are due to my sister Suzanne, deceased brother Brian, mother Mary, and deceased father Ron who have always encouraged and provided the means for me to learn and thrive.

Finally, well in excess of a thousand hugs are slated for my wife Samantha for her unswerving love.

TABLE OF CONTENTS

Page

Page

LIST OF FIGURES

Figure Page

Figure Page

ABSTRACT

Sigma-Delta modulators are among the key data conversion components in digital audio and multimedia systems. Power electronic converters transform power from one form to another by means of power semiconductor devices. For instance, an electric vehicle is propelled by an ac motor which derives its power from a dc battery. The dc-to-ac conversion is afforded by a power electronic converter. In this dissertation, we demonstrate the strong commonality between sigma-delta modulators and power electronic converters, and exploit this to invent, analyze, and build a new "quieter" and more efficient power electronic converter. Applications of this technology include electric submarines and vehicles, solar distribution systems, and wind turbines.

A novel application and generalization of sigma-delta modulation has emerged in the area of high frequency power electronics. A conventional sigma-delta modulator with scalar signals and binary quantizer is generalized to the hexagonal sigma-delta modulator which comprises vector signals and a hexagonal quantizer. Indeed, power electronic switching states may be thought of as determining the quantizer outputs. The output spectrum is a key performance measure for both communications and power electronics. This dissertation analytically derives the interesting output spectrum of the hexagonal sigma-delta modulator with a constant input using ergodic theory and Fourier series on the hexagon. The switching rate of the modulator is important for power electronic design. Formulas for the average switching rate are derived for constant and slowly varying sinusoidal inputs. Design techniques from communications such as white noise spectral analysis are generalized and applied to analyze the sigma-delta designs so that the noise can be shaped to

design requirements and a range of interpolative sigma-delta modulator designs from communications can be drawn upon. Hardware and simulation results demonstrate significantly improved spectral characteristics over prior work. The hexagonal sigma-delta modulator is patented and has been implemented in spectrally demanding commercial power electronic products.

Chapter 1

Introduction

Numerous advances in $\Sigma\Delta$ modulation technology have recently appeared in the communications literature. This dissertation generalizes and applies these improvements to the analysis and design of $\Sigma\Delta$ modulators for high frequency power electronic systems. The system of $\Sigma\Delta$ modulation originated in the early Sixties [1, 2, 3, 4] and has received significant attention over the past decade as an attractive alternative to conventional analog-to-digital converters [5, 6].

$\Sigma\Delta$ modulators or, more generally, oversampled analog-to-digital converters achieve the performance of high resolution quantizers by using low resolution quantizers in a feedback loop with linear filtering. These converters modulate an analog signal into a simple code, usually a single bit, at a frequency much higher than the Nyquist rate. In this manner, the modulator can trade resolution in time for resolution in amplitude as well as employ simple and relatively high-tolerance analog components [7, 8, 9, 6].

In power electronics, switching converters can also be viewed as analog-to-digital converters wherein an analog reference is coded into a low-resolution set of discrete switching states [10]. Moreover, switching converters typically switch at frequencies well in excess of the Nyquist rate. Therefore $\Sigma\Delta$ modulation techniques are pertinent. Indeed $\Sigma\Delta$ modulators have been applied successfully to systems such as resonant dc link converters (RDCL) wherein the discrete timing of the circuit switching precludes the use of conventional modulation techniques such as pulse-width modulation (PWM) [10, 11]. Resonant link converters use zero voltage switching to limit switching losses and attain relatively high switching frequencies [12].

The main analogy we exploit is with the methods in communications theory of converting (modulating) an analog signal to a digital signal with a quantizer and subsequently (after transmission) converting (demodulating) the digital signal back to analog form. For instance, a voltage source converter applies one of a finite set of discrete voltages on the converter output. The converter output is then passed through an analog low-pass filter that removes the modulation frequencies thereby demodulating the discrete voltages back to analog form. In both communications and power electronics, an aim is to design the system so that the input signal is transmitted with minimal distortion.

One consequence of this interpretation is that the power electronic switching states determine the possible "digitized states" or quantizer outputs. That is, the structure of the quantizer is determined by the power electronic circuit. For example, the conventional voltage source inverter (VSI) [13] of Fig. 1.1 has seven switching states which correspond to the seven output vectors in Fig. 1.2. We assume balanced three-phase signals represented by vectors with three coordinates which sum to zero. The outputs of the VSI are the line-to-neutral voltages which may equal one of seven possible values according to the switch state. These seven space vectors are shown as dots in Fig. 1.2 and can be thought of as the possible output vectors of a quantizer. Here we choose the quantizer so that a quantizer input vector u maps to the dot nearest to u. The broken lines in Fig. 1.2 delimit the regions which map to each dot. This "hexagonal" vector quantizer is a nearest neighbor quantizer and is well known in communications [14, 15]. Moreover, this quantizer is optimal in the sense that the mean-square error from input to output is minimized [14]. Viewing high frequency power electronic circuits as contributing to quantization allows them to be regarded as part of the modulator topology. It follows that noise-shaping methods of filter design may be applied to optimize the spectral characteristics.

To apply the conventional $\Sigma\Delta$ architecture with binary quantization to three phase converters requires some generalization. First, the output voltages of the VSI are limited to a set of seven output vectors which form a truncated hexagonal lattice. If we assume a nearest neighbor partition as in the binary case, the appropriate generalization is the truncated hexagonal vector quantizer

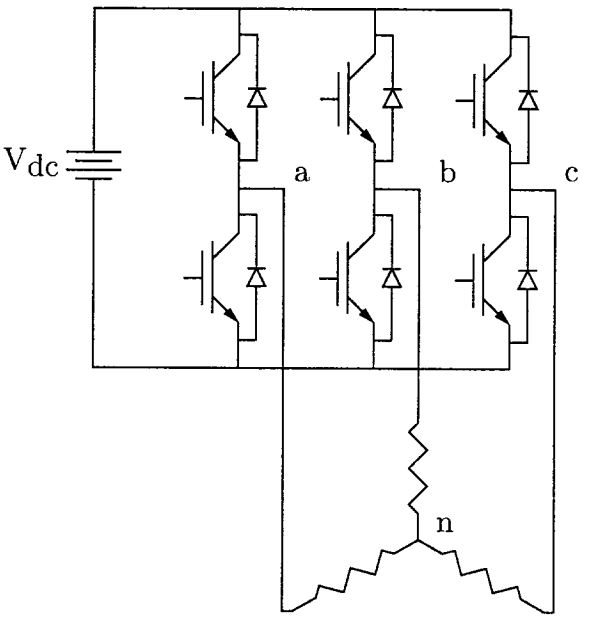

Figure 1.1 Voltage source inverter.

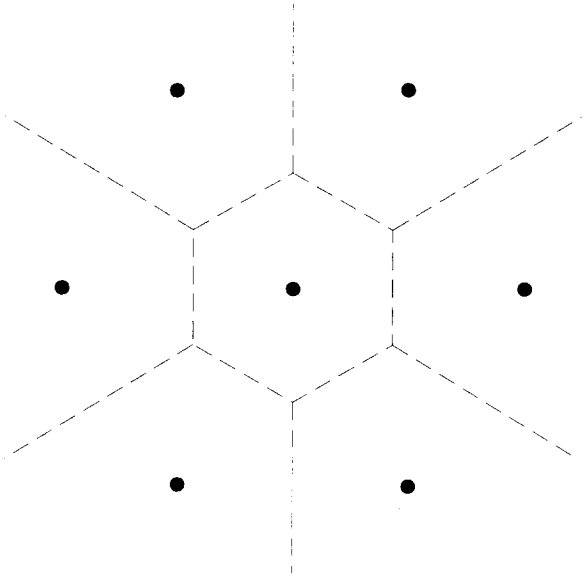

Figure 1.2 Voltage source inverter output states.

discussed above. Second, all modulator signals are augmented from scalar quantities to vectors and a vector integrator replaces the scalar integrator.

1.1 Motivations

There has been extensive design and analysis of scalar $\Sigma\Delta$ modulators for applications in communications and signal processing [5]. Also vector quantization is applied (but not to $\Sigma\Delta$ modulation) in a number of applications in signal processing [16]. The power electronic application combines specific vector quantizers with $\Sigma\Delta$ modulation and requires a significant generalization of the scalar work. Of course, vector quantization can be used in $\Sigma\Delta$ modulation simply by applying scalar $\Sigma\Delta$ modulation to each component; but the analysis of these systems is straightforward. In contrast, the hexagonal quantizer is not the Cartesian product of two scalar quantizers, so that the required generalization is not trivial. The vector generalization motivated by the power electronic application is natural enough in communications and signal processing since the nearest neighbor quantizer is one of the simplest vector quantizers. However, it appears that the use of hexagonal quantizers in $\Sigma\Delta$ modulators has not been studied previously and that this type of generalization has not been explored.

1.2 Approaches

The central component of a $\Sigma\Delta$ modulator is a quantizer, a device that maps real numbers into a finite set of possible representative values, often as few as two. Quantization is a nonlinear operation and thus rigorous analysis can be difficult. Incorporating a quantizer in a linear system with feedback as in the case of $\Sigma\Delta$ modulators renders the analysis challenging.

Two different approaches for analyzing $\Sigma\Delta$ modulators have evolved: approximate methods based on the results of Bennett [17], and exact analysis. In the first approach, one tries to approximate the quantization noise by choosing an input-independent additive noise source having a similar long-term sample distribution and power spectrum. The simplest noise model is white noise with a uniform distribution. Under such an approximation, the nonlinear $\Sigma\Delta$ modulator is modeled as a linear system, and the performance can readily be derived by using well-known linear system techniques. Moreover, approximate methods have been a key tool in practical design and have predicted many aspects of system behavior to a sufficient degree. Some of the properties agree reasonably well with simulation results [9, 18]. However, two notable failures of the linear model predictions are the generation of idle-channel tones and modulator instability [6].

Exact analysis was first applied successfully to discrete-time single-loop $\Sigma\Delta$ modulators with dc input [19, 20]. Instead of assuming the memoryless and uniformity characteristics, this approach derives the true quantizer noise behavior by solving a system of nonlinear difference equations, and then determining the noise statistics and power spectrum. The major conclusion is that the quantizer noise, even though uniformly distributed, is not white. In fact, the quantizer noise and output of single-loop $\Sigma\Delta$ modulators have discrete power spectra, which consists of spectral spikes whose frequency location depend in a complex way on the system input [21]. This suggests that the single-loop system is unfavorable; besides, the discrete nature of the spectra may be subjectively undesirable for certain applications such as digital audio.

Several researchers have applied exact analysis methods to scalar $\Sigma\Delta$ modulators to describe their behavior, predict their performance, and help develop improved systems. These works share the common goal of avoiding unjustified application of the white noise approximation. Powerful

techniques from ergodic theory have been deployed by Gray [19, 21], Delchamps [22, 23], and He et al. [24] to derive exact formulas for the spectra of scalar modulators for various inputs. Of related interest are the works of Kieffer [25] on stability and convergence of one-bit quantizers, and the work of Hein and Zakhor [26].

In this dissertation, we build on these exact analyses to derive the spectrum of a vector $\Sigma\Delta$ modulator with a hexagonal quantizer and a constant input. To simplify our analysis of this highly nonlinear system, we make two assumptions. The first assumption is that the modulator input is constant. While sinusoidal waveforms are also commonly used to test the system performance, the constant input is a useful idealization of slowly varying waveforms. The second assumption is that there is no overload in the internal quantizer. This can be accomplished by limiting the magnitude of the modulator input (i.e., dynamic range).

A key aspect of modulator performance is the output spectrum. Despite its complexity, we show in this dissertation that exact calculation of the output spectrum can be done using results from ergodic theory and Fourier analysis. In this approach, the nonlinear discrete dynamical system representing the modulator is thought of as iterated shifts on a torus and the typical statistics of the process may be computed by integration over the torus or subsets of the torus. The generic case of the spectrum calculation first appeared in our conference paper [27].

Switching rate is an important performance measure in power electronic design since device switching loss is directly proportional to the switching rate. We derive the average switching rate for the scalar and hexagonal $\Sigma\Delta$ modulators with generic constant inputs and then extend this calculation to slowly varying sinusoidal inputs.

Rigorous analysis of $\Sigma\Delta$ modulators is challenging because the quantizer nonlinearity occurs inside a feedback loop. However an approximate approach based on the results of Bennett [17] is very useful for many practical design purposes [9, 18, 28, 29]. In this approach, the quantization noise is approximated by an input-independent additive noise source having a similar long-term sample distribution and power spectrum. The simplest noise model is white noise with a uniform distribution. Under such an approximation, the nonlinear $\Sigma\Delta$ modulator becomes a linear system with a stochastic input, and the performance can easily be derived.

For a single-loop scalar $\Sigma\Delta$ modulator without overload, the white noise approximation gives good estimates of the mean-square quantization error [30, 31] and signal-to-noise ratio (SNR). On the other hand, the white noise approximation fails to predict idle tones in the output spectrum [21] or modulator instability [26]. However, the white-noise approximation is exact for higher order scalar $\Sigma\Delta$ architectures provided the quantizer does not overload [21].

We extend the conventional white noise analysis of the scalar $\Sigma\Delta$ modulator to the hexagonal $\Sigma\Delta$ modulator and thereby derive useful design graphs and formulae. We use analysis and simulation to compare the single-loop and double-loop hexagonal $\Sigma\Delta$ modulators in terms of spectra and switching rate and demonstrate the advantages of the double-loop hexagonal $\Sigma\Delta$ modulator [32].

There is considerable advantage in using analytic formulas for the output spectrum and switching rate in design because simulation of data with complicated nonperiodic structures has difficulties of run time, data processing and limited insight into the nature of the process and the parameter dependencies.

1.3 Literature Review

Although the *methods* used in this dissertation are a generalization of exact analysis methods for scalar $\Sigma\Delta$ modulators in communications theory, much of the current technological *motivation* for the results comes from power electronics. Therefore, while the hexagonal $\Sigma\Delta$ modulator may well find applications outside power electronics, it is appropriate to conclude this introduction with a review of the applications of oversampled analog-to-digital converters to power electronics.

Oversampled analog-to-digital converters have been employed in power electronics for nearly two decades. However, attention to these converters has been sparse in comparison to the vast literature for pulse width modulators (PWM). The first reported application of an oversampled converter (delta modulator) was to a conventional three phase transistor inverter wherein the integration of the output voltage was calculated via the output inductors. The output current closed the feedback loop and thus could be controlled [33]. This so-called current controlled delta modulator exhibited a non-zero steady-state output current error which was improved by the addition of an integrator in the forward path [34].

The invention of the soft switching resonant dc link converter by Divan [12] fostered interest in $\Sigma\Delta$ modulators since they both require constrained switching instants. Studies of three-fold scalar $\Sigma\Delta$ modulators applied to resonant link inverters that considered their spectral performance and harmonic distortion using simulation, experiment, and basic analysis were reported in [35]. The three-fold $\Sigma\Delta$ modulator uses three identical independent scalar modulators to control each of the three inverter leg voltages. The three-fold modulator has reduced dynamic range compared to the hexagonal $\Sigma\Delta$ modulator. A zero output voltage state (i.e. all switches high/low) was introduced in [11] to obtain adjacent state switching. This so-called modified $\Sigma\Delta$ modulator is a three-fold $\Sigma\Delta$ modulator with the provision that non-adjacent states are overridden by a zero state. This work differs from the hexagonal $\Sigma\Delta$ in that the zero vector is not chosen unless a non-adjacent state is selected. Seidl [36] derived the hexagonal quantizer based on its one-step ahead optimality properties (minimum squared error) and developed a neural network delta modulator employing the hexagonal quantizer. An alternative to current controlled delta modulators using a one-step ahead minimization of the infinity norm of the current error was proposed in [37]. Another possibility based on sliding modes [38] is presented in [39]. Attempts to combine $\Sigma\Delta$ modulation with space vector modulation [13] are developed in [40] and [41]. Summaries of the application of current controlled delta modulators and (to a lesser extent) $\Sigma\Delta$ modulators to resonant link inverters prior to 1994 are found in [42, 36, 40]. The use of $\Sigma\Delta$ modulators for control of electromagnetic interference (EMI) in switch-mode power supplies is considered in [43].

A simple coherent analysis of $\Sigma\Delta$ modulators applied to resonant link converters was reported by Mertens in [44]. This work drew from the basic reference in communications for the behavior of quantization noise with dc input of Candy and Benjamin [8]. They extended methods of Iwersen [45] from Δ modulation. Their approach was based on an approximate continuous time model for a $\Sigma\Delta$ modulator and their results well matched experimental results (for a continuous time system). They applied their approximations to evaluate the mean squared error when an ideal low-pass filter is used as a decoder. Iwersen applied Fourier series expansion of the quantizer error function to a specific input to obtain a Fourier series for the error sequence from which the spectrum was deduced [45].

In 1998 Nieznański [46] compared the hexagonal $\Sigma\Delta$ modulator to the modified $\Sigma\Delta$ modulator of [11] and the threefold-scalar $\Sigma\Delta$ modulator [35, 42] and showed that the hexagonal $\Sigma\Delta$ modulator has lower distortion power and device switching rate. This work builds on the comparisons made in [40]. Via simulation, this work showed the hexagonal $\Sigma\Delta$ to have lower distortion power and device switching rate. Additionally, this study compared the hexagonal $\Sigma\Delta$ to space vector PWM [13]. For inputs less than 90%, the space vector PWM was shown to outperform the hexagonal $\Sigma\Delta$ in the sense that it requires lower device switching frequency to obtain a given spectral performance. However, for inputs exceeding 90% the situation is reversed.

In 1995 we introduced [10] and patented [47] the hexagonal $\Sigma\Delta$ modulator as well as extensions to double-loop and interpolative hexagonal $\Sigma\Delta$ modulators. As this technology represented a significant improvement in spectral performance of resonant dc link converters, a hardware platform was rapidly developed for deployment in commercial applications by SoftSwitching Technologies, Madison, Wisconsin. Notable successes of the technology include:

- A 2.4 MVA permanent magnet motor drive for a "silent", ultra-low total-harmonic-distortion (THD), high-density, and high-efficiency Navy electric submarine (*Cutthroat*).
- A 200 kVA hybrid active filter for an induction heating application contracted by Tommie Inc.
- A 30 kW regenerative drive for elevators contracted by Yaskawa Electric Inc.
- A 250 kVA bidirectional wind turbine contracted by the University of Massachusetts.
- A 175 kVA frequency converter for commercial aircraft applications.
- A 175 kVA bidirectional pump drive for naval applications.
- A 175 kVA solar distribution/generation system.
- A 70 kW electrical vehicle drive system contracted by General Motors Inc.
- A 200 kVA bidirectional automatic-voltage-regulator (AVR) for a plastics application.

A novel insight put forth in [10] is that a power electronic circuit may be thought of as an analog-to-digital converter in which the analog input is the signal to be synthesized and the quantized digital output is the state of the circuit switches. One consequence of this interpretation is that the power electronic switching states determine the possible "digitized states" or quantizer outputs. Similarly, other circuits such as the matrix converter, multilevel converters, and multiphase converters define particular quantizer outputs.

We have also analytically derived the exact output spectrum (no white noise approximation) of the hexagonal $\Sigma\Delta$ modulator with a constant input using ergodic theory and hexagonal Fourier series [48, 32, 27]. The switching rate of the modulator is important for power electronic design and formulas for the average switching rate are derived for constant and slowly varying sinusoidal inputs [48].

1.4 Overview

Chapter 2 Considers $\Sigma\Delta$ modulation and quantization in the context of power electronics.

Chapter 3 Develops and rigorously analyzes the model of the classical single-bit $\Sigma\Delta$ modulator with constant input.

Chapter 4 Derives long-term statistics of the hexagonal $\Sigma\Delta$ modulator driven by a constant input as well as calculates the Fourier coefficients for the hexagonally distributed error function for the hexagonal $\Sigma\Delta$ modulator.

Chapter 5 Calculates a closed form formula for the autocorrelation of the quantization noise for the hexagonal $\Sigma\Delta$ modulator. The autocorrelation formula is numerically validated against the result of Chapter 4.

Chapter 6 Derives the average switching rate for the single-bit $\Sigma\Delta$ modulator and the hexagonal $\Sigma\Delta$ modulator. Also, we determine the switching rate for slowly varying inputs.

Chapter 7 Reviews the linear analysis of the single-bit $\Sigma\Delta$ modulator, and then extends these results to the hexagonal $\Sigma\Delta$ modulator.

Chapter 8 Presents simulation results confirming the analytic results for the quantizer error and output spectra, and the average switching rate of the hexagonal $\Sigma\Delta$ modulator. Hardware implementations of various hexagonal $\Sigma\Delta$ modulators for power electronic converters are presented. These modulators are currently manufactured for spectrally demanding commercial applications.

Chapter 9 Finally, conclusions are made and possible directions for further work are indicated.

Chapter 2

Application of $\Sigma\Delta$ Modulation to Power Electonics

This chapter explains a conventional scalar $\Sigma\Delta$ modulator [5], and how a half-bridge converter may be embedded in the modulator structure. These ideas are then generalized to the vector modulator of central interest in this dissertation.

2.1 Scalar $\Sigma\Delta$ Modulator

The simplest form of a $\Sigma\Delta$ modulator is shown in Fig. 2.1. x is the input signal, u is the integrator state and y is the latch output. The comparator is thought of as a quantizer whose output $q(u)$ is ± 1 according to the the sign of the integrator state u. The latch samples the comparator or quantizer output $q(u)$ at the sampling frequency f_s and holds that value until the next sampling instant.

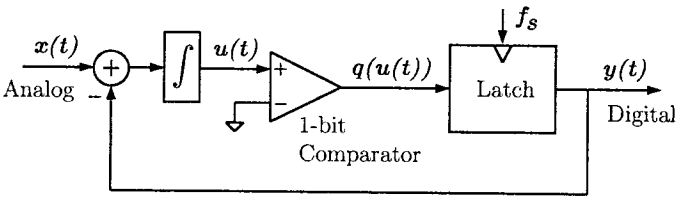

Figure 2.1 Conventional sigma-delta modulator.

Intuitively, the $\Sigma\Delta$ modulator uses feedback to lock onto a band-limited input signal $x(t)$. As explained in [29], "Unless the input signal $x(t)$ exactly equals one of the discrete quantizer output levels, a tracking error results. The integrator accumulates the tracking error over time and the quantizer and latch feed back a value that will minimize the accumulated tracking error. Thus the quantizer output $y(t)$ toggles about the input signal $x(t)$ so that the average quantizer output

is approximately equal to the average of the input." A typical $\Sigma\Delta$ modulator output waveform (reference superimposed) is shown in Fig. 2.2.

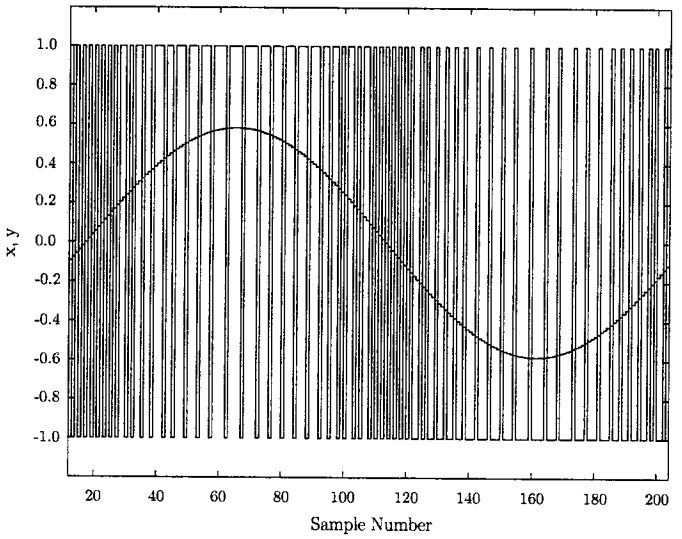

Figure 2.2 Waveform of a $\Sigma\Delta$ modulator.

To illustrate how a power electronic circuit can be embedded in a $\Sigma\Delta$ modulator, consider the modulator for the half-bridge converter shown in Fig. 2.3. In this arrangement the gating circuitry and half-bridge are embedded into the loop following the latch in Fig. 2.1. The comparator and latch set the switch state for each sampling period according to the sign of the comparator input u at the sampling instant. The switch state impresses the voltage $\pm V$ on the output, $y(t)$. Since Fig. 2.3 and Fig. 2.1 are different implementations of the same overall quantizing and latch functions, the corresponding modulators have identical behavior. Thus, by taking the input signal $x(t)$ to be the desired output voltage, the actual output voltage $y(t)$ will approximate the desired output voltage. As will be seen, this approximation can be improved by generalizing the integrator in Fig. 2.1 to a linear filter or by increasing the sampling rate f_s.

2.2 Hexagonal $\Sigma\Delta$ Modulator

We now consider a vector $\Sigma\Delta$ modulator which may be applied to a voltage source inverter (VSI) (Fig. 1.1). As detailed in the introduction, the outputs of the VSI are the line-to-neutral

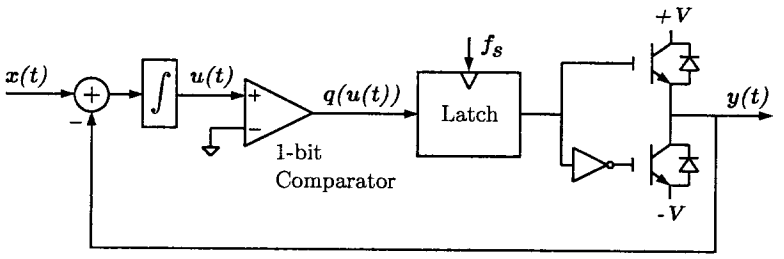

Figure 2.3 Half-bridge embedded in ΣΔ modulator loop.

voltages which may equal one of seven possible values according to the VSI switch state. These seven space vectors can be considered as quantizer outputs and are shown as dots in Fig. 1.2. The action of the quantizer is to map the the delimited regions to the nearest dot (neighbor). Hence, this "hexagonal" vector quantizer is an example of a nearest neighbor quantizer [14, 15].

Generalizing the ΣΔ modulator with binary quantization to the VSI entails two modifications. First, the nearest neighbor binary quantizer is generalized to the nearest neighbor hexagonal quantizer of Fig. 1.2. Second, all modulator signals are augmented from scalars to vectors, and a vector integrator replaces the scalar integrator. In an analogous manner to the half-bridge circuit of Section 2.1, the VSI may be embedded in the vector ΣΔ loop with hexagonal quantization (Fig. 2.4). We call the system of Fig. 2.4 with the VSI omitted a hexagonal ΣΔ modulator.

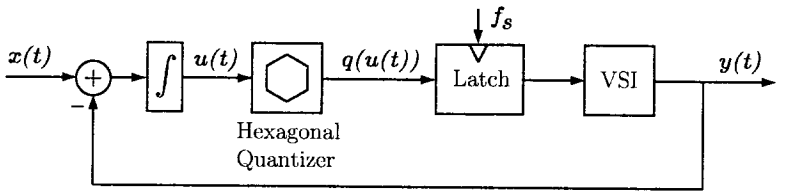

Figure 2.4 VSI embedded in hexagonal ΣΔ modulator loop.

A typical output line-neutral waveform (reference superimposed) and spectrum for the hexagonal ΣΔ modulator are shown in Fig. 2.5 and Fig. 2.6 respectively. The oversampling ratio is 64 and the input amplitude is 80% of full-scale linear range. The oversampling ratio (OSR) is defined as ratio of the switching (sampling) frequency, f_s to the reference Nyquist frequency, $2f_o$ ($f_s/2f_o$). For practical converters, the OSR typically ranges from 16 to 256.

We call the frequency band $0 \leq f < f_0$ the baseband; it includes the frequency of the input signal and the band over which we wish to reduce noise in the output. The baseband is chosen according to the application specifications. The input x_n is sampled by the modulator at a frequency much higher than the baseband.

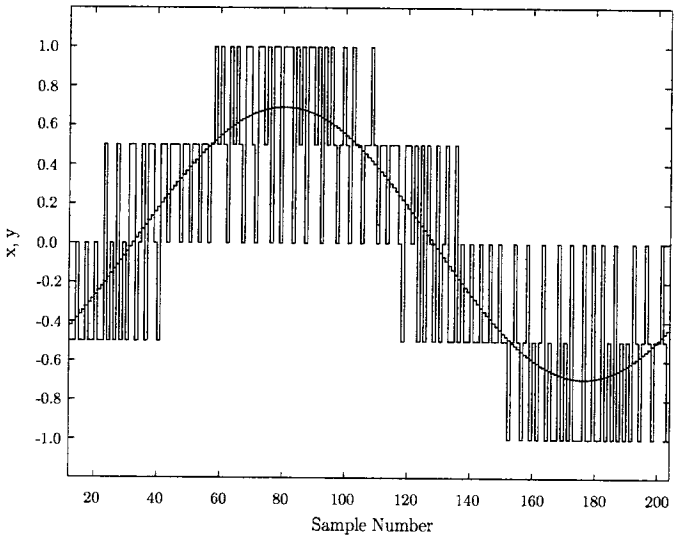

Figure 2.5 Waveform of a hexagonal $\Sigma\Delta$ modulator.

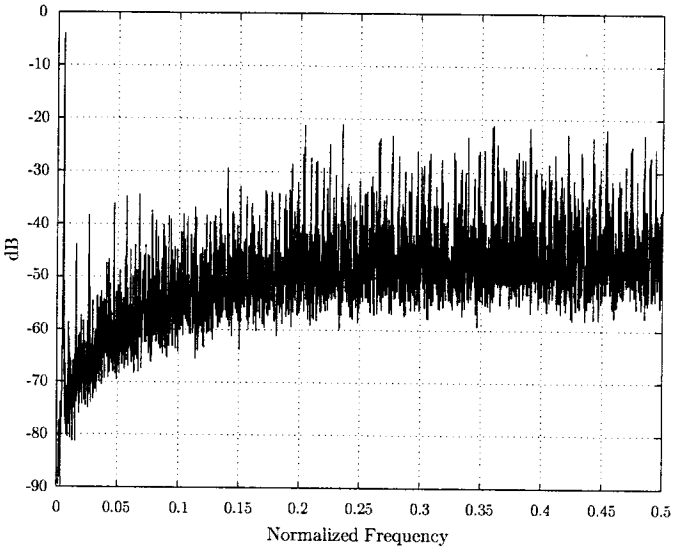

Figure 2.6 Spectrum of a hexagonal $\Sigma\Delta$ modulator.

Chapter 3

Single-Bit $\Sigma\Delta$ Modulator

This chapter reviews the spectral calculation for a single-bit $\Sigma\Delta$ modulator with a generic constant input. In this context, the single-bit modulator has been studied extensively by Gray, Delchamps, and He et al [20, 19, 22, 23]. The purpose of the section is to explain in a simpler context the spectral calculation method that is used for the hexagonal case.

3.1 Discrete-Time Model

A conventional discrete-time single-loop $\Sigma\Delta$ modulator is shown in Fig. 3.1 where $\beta, u, e \in \mathbb{R}$ and q is the single-bit quantizer

$$q(x) = \begin{cases} 1/2 & \text{if } x \geq 0, \\ -1/2 & \text{otherwise.} \end{cases}$$

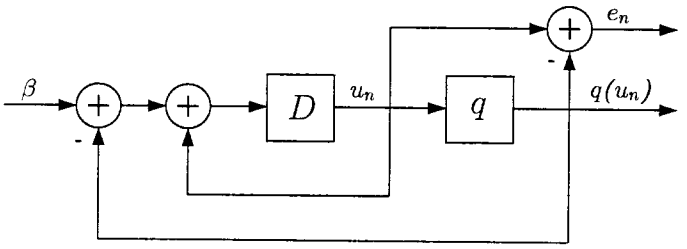

Figure 3.1 Discrete-time single-bit or hexagonal $\Sigma\Delta$ modulator. D: unit delay. q: single-bit or hexagonal quantizer.

From Fig. 3.1, one can write the following difference equations that describe the $\Sigma\Delta$ modulator:

$$u_{n+1} = \beta + u_n - q(u_n) \tag{3.1}$$

where β is the discrete-time input, u_n is the modulator state, and $q_n = q(u_n)$ is the quantizer output at time n.

A key process in the analysis is the quantizer error sequence defined by

$$e_n = e(u_n) = u_n - q_n \tag{3.2}$$

Using (3.1) and (3.2), the state and output processes can be expressed in terms of the input and the error sequence:

$$u_{n+1} = e_n + \beta \tag{3.3}$$

$$q_{n+1} = e_n - e_{n+1} + \beta \tag{3.4}$$

By substituting (3.3) into (3.2), the error sequence satisfies the nonlinear difference equations:

$$\begin{aligned} e_0 &= e(u_0) \\ e_{n+1} &= e(e_n + \beta), \quad n = 0, 1, \ldots \end{aligned} \tag{3.5}$$

3.2 Solution of the Difference Equation

The quantizer error defined by $e(u) = u - q(u)$ is graphed in Fig. 3.2 as a function of the quantizer input u. We see that if the quantizer input u is confined to the interval $[-1, 1]$, then the error will be bounded in magnitude by $1/2$. If the input is outside that region, then the error magnitude will be larger than $1/2$, and the quantizer is said to be overloaded. Thus $[-1, 1]$ is called the *no-overload region.*

We assume the no-overload condition that $|\beta| \leq 1/2$ and $|u_0| \leq 1$. It follows that $|e_n| \leq 1/2$ and $|u_n| \leq 1$ for $n = 0, 1, \ldots$ [20]. Then the quantizer error can be expressed as [20]

$$e(u) = \langle u \rangle - \frac{1}{2}, \quad \text{for } u \in [-1, 1] \tag{3.6}$$

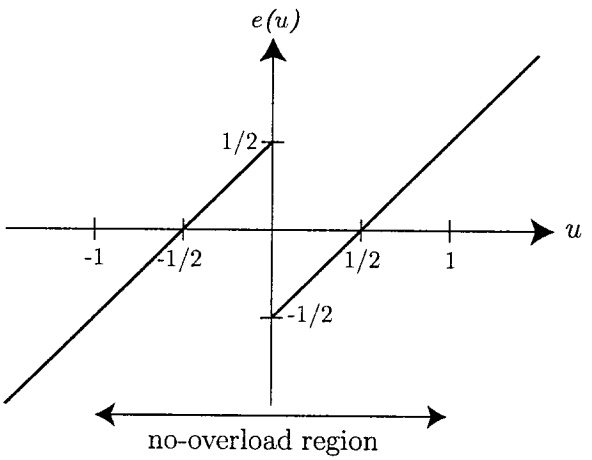

Figure 3.2 Quantizer error.

where $\langle r \rangle$ is the fractional part of r; that is, $\langle r \rangle = r - \lfloor r \rfloor$, where $\lfloor r \rfloor$ denotes the largest integer not greater than r.

For a system with no-overload, (3.5) becomes

$$e_{n+1} = \langle e_n + \beta \rangle - \frac{1}{2}, \quad n = 0, 1, \ldots \tag{3.7}$$

For convenience define

$$y_n = y(u_n) = \frac{1}{2} + e(u_n), \qquad u_n \in [-1, 1] \tag{3.8}$$

so that (3.7) becomes

$$y_{n+1} = \langle y_n + \beta' \rangle, \quad n = 1, 2, \ldots \tag{3.9}$$

where $\beta' = \beta - \frac{1}{2}$.

The solution to (3.9) is [20]

$$y_n = \langle y_0 + n\beta' \rangle \tag{3.10}$$

3.3 Spectrum of the Quantizer Error

The autocorrelation function of the y sequence is defined as

$$R_y(n) = \lim_{L \to \infty} \frac{1}{L} \sum_{k=0}^{L-1} y_k \, y_{k+n} \tag{3.11}$$

whenever the limit exists. Use (3.10) to obtain

$$\begin{aligned} R_y(n) &= \lim_{L \to \infty} \frac{1}{L} \sum_{k=0}^{L-1} \langle y_0 + k\beta' \rangle \, \langle y_0 + k\beta' + n\beta' \rangle \\ &= \lim_{L \to \infty} \frac{1}{L} \sum_{k=0}^{L-1} \langle y_0 + k\beta' \rangle \, \langle \langle y_0 + k\beta' \rangle + n\beta' \rangle \end{aligned} \tag{3.12}$$

A classical result in ergodic theory due to Weyl is [49]

Theorem 3.1 If f is an Riemann-integrable function, $\beta \in \mathbb{R}$ is irrational, and $r \in \mathbb{R}$ then

$$\lim_{L \to \infty} \frac{1}{L} \sum_{k=0}^{L-1} f(\langle \beta k + r \rangle) = \int_0^1 f(s) ds$$

This phenomenon is referred to as the equidistribution of the sequence since the sequence $\langle \beta k + r \rangle$ uniformly fills the unit interval and the sums approach an integral in the limit.

We assume β' irrational and apply Theorem 3.1 to $f(s) = s\ \langle s + n\beta' \rangle$ in (3.12) to obtain

$$R_y(n) = \int_0^1 \langle s \rangle \langle s + n\beta' \rangle\, ds \tag{3.13}$$

Let $f, g \in L^2([0,1))$ have Fourier coefficients $\hat{f}_p$, $\hat{g}_p$, $p \in \mathbb{Z}$. Then Parseval's formula is

$$\int_0^1 f(s)\, g^*(s) ds = \sum_{p\in\mathbb{Z}} \hat{f}_p\, \hat{g}_p^* \tag{3.14}$$

The function $\langle\ \rangle \in L^2([0,1))$ is periodic and has Fourier series

$$\langle u \rangle = \sum_{p\in\mathbb{Z}} c_p e^{i2\pi pu} \tag{3.15}$$

where

$$c_p = \int_0^1 \langle u \rangle\, e^{-i2\pi pu} du = \begin{cases} \frac{1}{2} & \text{if } p = 0, \\ \frac{i}{2\pi p} & \text{if } p \neq 0 \end{cases}$$

The Fourier coefficients of $g(x) = \langle x + n\beta' \rangle$ are $c_p e^{i2\pi pn\beta'}$. Applying Parseval's formula to (3.13) gives

$$R_y(n) = \sum_{p\in\mathbb{Z}} c_p c_p^* e^{-i2\pi pn\beta'} = \sum_{p\in\mathbb{Z}} |c_p|^2 e^{i2\pi p\beta' n} \tag{3.16}$$

Since $\sum_{p\in\mathbb{Z}} |c_p|^2 = \frac{1}{3}$, the series (3.16) for $R_y(n)$ is absolutely summable and this implies uniform convergence of the series (3.16) with respect to n. Since almost periodic sequences are the uniform limit of trigonometric polynomials, $R_y(n)$ is almost periodic [50].

A complex valued sequence g_n defined for $n \in \mathbb{Z}$ is called *almost periodic*, if for any $\epsilon > 0$ there exists a trigonometric polynomial $T_\epsilon(n)$, such that

$$|g_n - T_\epsilon(n)| < \epsilon, \qquad n \in \mathbb{Z} \tag{3.17}$$

An alternate definition for an *almost periodic* sequence g_n is that if for every $\epsilon > 0$ it is possible to find a positive number $l(\epsilon)$ such that every interval of length $l(\epsilon)$ contains at least one $m \in \mathbb{Z}$ such that $|g_{n+m} - g_n| < \epsilon$ for $n \in \mathbb{Z}$ [50].

We now compute the spectrum S_y of the almost periodic sequence R_y. It is known from harmonic analysis that the spectrum of an almost periodic sequence is discrete (pure point). The pure point part of the spectrum S_y may be recovered from the autocorrelation sequence $R_y(n)$ for any point $\lambda_p \in [0,1)$ by the mean value of the almost periodic sequence $R_e(n)e^{-i2\pi\lambda_p n}$ [51, 22].

$$\begin{aligned} S_y(\{\lambda_p\}) &= \lim_{N\to\infty} \frac{1}{2N+1} \sum_{n=-N}^{N} R_y(n) e^{-i2\pi\lambda_p n} \\ &= \lim_{N\to\infty} \frac{1}{2N+1} \sum_{n=-N}^{N} \sum_{p\in\mathbb{Z}} |c_p|^2 e^{i2\pi(p\beta'-\lambda_p)n} \\ &= \sum_{p\in\mathbb{Z}} |c_p|^2 \lim_{N\to\infty} \frac{1}{2N+1} \sum_{n=-N}^{N} e^{i2\pi(p\beta'-\lambda_p)n} \end{aligned} \tag{3.18}$$

The interchange of summations is justified since $\sum_{p\in\mathbb{Z}} |c_p|^2 < \infty$. Thus,

$$S_y(\{\lambda_p\}) = \begin{cases} 0 & \text{if } p\beta' \neq \lambda_p \mod 1, \\ |c_p|^2 & \text{if } p\beta' = \lambda_p \mod 1. \end{cases} \tag{3.19}$$

The numbers $\{\lambda_p, p \in \mathbb{Z}\}$ are called the Bohr-Fourier frequencies of the sequence $R_y(n)$, and $|c_p|^2$ are the Bohr-Fourier coefficients of $R_y(n)$. Rewriting (3.19) and using $y = 1/2 + e$ the spectrum of the quantization error is [19, 23]

$$S_e(\omega) = \sum_{\substack{p\in\mathbb{Z} \\ p\neq 0}} |c_p|^2 \delta(\omega - \langle p\beta' \rangle) \tag{3.20}$$

According to (3.4), the quantizer output q is obtained by differencing e and adding β. Hence standard linear system Fourier analysis techniques can be applied to obtain from (3.20) the spectrum of the quantizer output q:

$$S_q(\omega) = \beta^2\delta(\omega) + 4\sum_{\substack{p\in\mathbb{Z} \\ p\neq 0}} |c_p|^2 \sin^2(\pi\omega)\delta(\omega - \langle p\beta' \rangle) \tag{3.21}$$

The output spectral density S_q is purely discrete having amplitudes $4\,|c_p|^2 \sin^2(\pi\omega)$ at frequencies $\langle p\beta' \rangle$ for $0 \neq p \in \mathbb{Z}$, and the square of the input at zero frequency.

3.4 Mean and Variance

This section computes the mean and variance of the quantizer error function for the single-bit $\Sigma\Delta$ modulator for a generic constant input.

We denote the long-term time average or mean and variance by

$$\overline{y} = \lim_{L\to\infty} \frac{1}{L} \sum_{k=0}^{L-1} y_k \tag{3.22}$$

$$\overline{y^2} = \lim_{L\to\infty} \frac{1}{L} \sum_{k=0}^{L-1} y_k^2 \tag{3.23}$$

respectively.

We now apply Theorem 3.1 to the sequence y_n of (3.10) to determine the desired statistics for an irrational input β. Taking $f(s) = s$ in Theorem 3.1, the mean of y is given by

$$\overline{y} = \int_0^1 s\, ds = \frac{1}{2} \tag{3.24}$$

and taking $f(s) = s^2$ the variance is

$$\overline{y^2} = \int_0^1 s^2\, ds = \frac{1}{3} \tag{3.25}$$

By the definition of y in (3.8), the mean and variance of the quantizer error sequence e_n are

$$\overline{e} = 0$$

$$\overline{e^2} = \frac{1}{12}$$

The quantizer output q_n is obtained by differencing e_n and adding x according to (3.4). Hence, the mean and variance of q_n are

$$\overline{q} = x$$

$$\begin{aligned}\overline{q^2} &= 2\,\overline{e^2} - 2R_e(1) + x^2 \\ &= \beta(1-\beta) + x^2\end{aligned}$$

If β is rational, then Weyl's formula may be replaced by a standard result from finite fields [19]; however, we will not pursue these results here.

Chapter 4

Hexagonal $\Sigma\Delta$ Modulator

This chapter describes mathematical underpinnings, including hexagonal coordinate systems, lattices and quantizers, and states the nonlinear difference equation for the hexagonal modulator. As a preliminary step we mathematically describe the hexagonal lattice and discuss its properties. We then proceed in a similar fashion to the single-bit modulator of the previous chapter.

A key aspect of modulator performance is the output spectrum. Despite its complexity, exact calculation of the output spectrum can be done using results from ergodic theory and Fourier analysis. In this approach the nonlinear discrete dynamical system representing the modulator is thought of as iterated shifts on a torus and the typical statistics of the process may be computed by integration over the torus. We performed these calculations for the generic constant input case and they generalize similar results for scalar $\Sigma\Delta$ modulators.

4.1 Hexagonal Lattices and Coordinates

It is convenient to define the plane $\mathcal{P} = \{(x, y, z)^t \in \mathbb{R}^3 \mid x + y + z = 0\}$, where t denotes transpose. Define $W : \mathbb{R}^2 \rightarrow \mathcal{P}$ and $V : \mathcal{P} \rightarrow \mathbb{R}^2$ to be

$$W = \begin{bmatrix} 1 & 0 \\ 0 & 1 \\ -1 & -1 \end{bmatrix}, \quad V = \frac{1}{3} \begin{bmatrix} 2 & -1 & -1 \\ -1 & 2 & -1 \end{bmatrix}. \tag{4.1}$$

VW is the identity on $\mathbb{R}^2$ and WV is the identity on $\mathcal{P}$.

The hexagonal lattice is $\Lambda = \bigcup\{Wk \mid k \in \mathbb{Z}^2\} = \mathcal{P} \bigcap \mathbb{Z}^3$. The large dots in Fig. 4.1 show points in Λ.

The dual of $\mathcal{P}$ is $\mathcal{P}^* = \{(x,y,z) \in \mathbb{R}^{*3} \mid x+y+z=0\}$. The lattice *dual* [14] to Λ is

$$\Lambda^* = \{p \in \mathcal{P}^* \mid p\lambda \in \mathbb{Z} \text{ for all } \lambda \in \Lambda\} = \bigcup \{qV \mid q \in \mathbb{Z}^{*2}\}$$

The vertices of hexagon H in Fig. 4.1 are points in Λ^*.

Vectors in $\mathcal{P}$ or Λ are written as column vectors and dual vectors in $\mathcal{P}^*$ or Λ^* are written as row vectors. For example, $n_a \in \mathcal{P}$ in Fig. 4.1 is the column vector $\frac{1}{3}(2,-1,-1)^t$. The columns of W generate Λ and the rows of V generate Λ^*.

The Voronoi cells (points closest to a given lattice point) of Λ are hexagons of side $\sqrt{2/3}$. Define the set H to be the interior of the Voronoi cell containing 0, together with a specific choice of 3 non-opposite hexagon sides and 2 opposite hexagon vertices. (These choices ensure that lattice translates of H tile the plane with no overlapping points.) H is the dark central hexagonal region of Fig. 4.1. The area of H is $|H| = \sqrt{3}$.

Define vectors n and $n^\perp$ by (see Fig. 4.1):

$$n_a = \frac{1}{3}\begin{pmatrix} 2 \\ -1 \\ -1 \end{pmatrix}, \quad n_b = \frac{1}{3}\begin{pmatrix} -1 \\ 2 \\ -1 \end{pmatrix}, \quad n_c = \frac{1}{3}\begin{pmatrix} -1 \\ -1 \\ 2 \end{pmatrix},$$

$$n_a^\perp = \begin{pmatrix} 0 \\ -1 \\ 1 \end{pmatrix}, \quad n_b^\perp = \begin{pmatrix} 1 \\ 0 \\ -1 \end{pmatrix}, \quad n_c^\perp = \begin{pmatrix} -1 \\ 1 \\ 0 \end{pmatrix}.$$

Also define $n_{-s} = -n_s$, $n_{-s}^\perp = -n_s^\perp$. Note that $n_s^t n_s^\perp = 0$, $|n^\perp| = \sqrt{2}$, and $|n| = \sqrt{2/3}$.

Coordinates $\beta_a^\perp, \beta_b^\perp, \beta_c^\perp$ for $\mathcal{P}$ are defined by

$$\beta_a^\perp = \beta \cdot n_a^\perp, \qquad \beta_b^\perp = \beta \cdot n_b^\perp, \qquad \beta_c^\perp = \beta \cdot n_c^\perp. \tag{4.2}$$

Coordinates p_a, p_b, p_c for $\mathcal{P}^*$ are defined by

$$p_a = pn_a, \qquad p_b = pn_b, \qquad p_c = pn_c. \tag{4.3}$$

It is convenient to define an ordered coordinate system for $\mathcal{P}$: Let $\beta_1^\perp, \beta_2^\perp, \beta_3^\perp$ be an ordering of $\beta_a^\perp, \beta_b^\perp, \beta_c^\perp$ chosen so that $|\beta_1^\perp| \geq |\beta_2^\perp| \geq |\beta_3^\perp|$. The ordered coordinates are a continuous,

non-differentiable function of the original coordinates. Also, the ordered coordinates satisfy the relation:

$$|\beta_1^\perp| = |\beta_2^\perp| + |\beta_3^\perp| \tag{4.4}$$

(4.4) is proved by noting that when $\beta_1^\perp$ is positive (say), $\beta_2^\perp$ and $\beta_3^\perp$ are necessarily negative; and that $\beta_1^\perp + \beta_2^\perp + \beta_3^\perp = 0$. We write $n_j^\perp = \beta_j^\perp / |\beta|$, $j = 1, 2, 3$ so that $\beta_j^\perp = \beta \cdot n_j^\perp$.

In the ordered coordinate system we may define with economy the various regions of Fig. 4.1:

$$H = \{x \in \mathcal{P} : \ |x_1^\perp| \leq 1\} \tag{4.5}$$

$$U = \{x \in \mathcal{P} : \ |x_2^\perp| \leq 1/2\} \tag{4.6}$$

$$S = \{x \in \mathcal{P} : \ |x_2^\perp| \leq 1\} \tag{4.7}$$

$$R = \{x \in \mathcal{P} : \ |x_1^\perp| \leq 3 \text{ and } |x_2^\perp| \leq 2\} \tag{4.8}$$

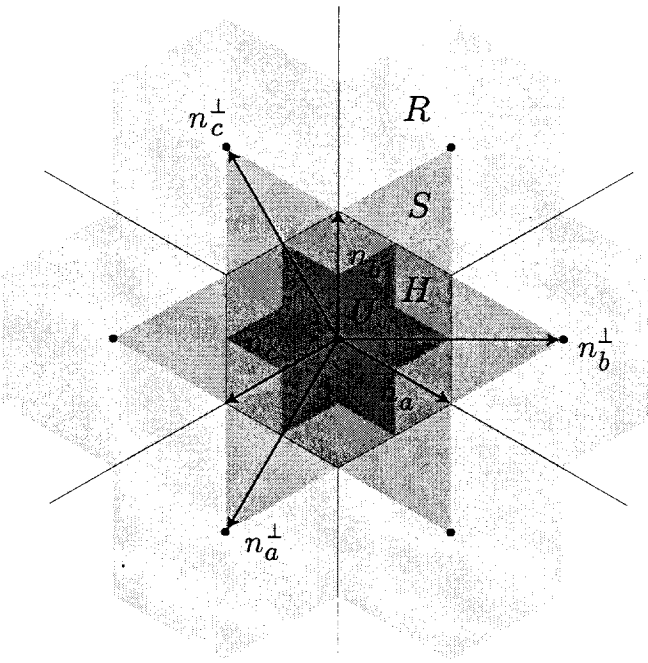

Figure 4.1 Hexagonal quantizer q and regions H, S, and R.

4.2 Hexagonal Quantizer and Discrete-Time Model

A function f on $\mathcal{P}$ is *hexagonally periodic* if $f(x+\lambda) = f(x)$ for all $\lambda \in \Lambda$. Define $\langle\!\langle\!\rangle\!\rangle : \mathcal{P} \to H$ as the identity on H and extend the definition of $\langle\!\langle\!\rangle\!\rangle$ to $\mathcal{P}$ by making $\langle\!\langle\!\rangle\!\rangle$ hexagonally periodic. One might call $\langle\!\langle\!\rangle\!\rangle$ "hexagonal part" since $\langle\!\langle\!\rangle\!\rangle$ generalizes to $\mathcal{P}$ the scalar fractional part $\langle\ \rangle$.

Let $x, y \in \mathcal{P}$. Then

$$\langle\!\langle x+y \rangle\!\rangle = \langle\!\langle \langle\!\langle x \rangle\!\rangle + y \rangle\!\rangle \tag{4.9}$$

Define the hexagonal lattice nearest neighbor quantization function q to be

$$q(x) = x - \langle\!\langle x \rangle\!\rangle \tag{4.10}$$

The nearest neighbor quantizer q is shown in Fig. 4.1. The input u to q is a point in the plane $\mathcal{P}$ and the output $q(u)$ is the nearest to u of the seven truncated hexagonal lattice points $\{0, \pm n_a^{\perp}, \pm n_b^{\perp}, \pm n_c^{\perp}\}$ in Fig. 4.1.

A discrete time hexagonal $\Sigma\Delta$ modulator is shown in Fig. 3.1. The signals β, u_n, q_n, and e_n are now interpreted as vectors in the plane $\mathcal{P}$.

The discrete-time model derivation exactly parallels that of section 3.1 and the error sequence satisfies the nonlinear difference equations:

$$\begin{aligned} e_0 &= e(u_0) \\ e_{n+1} &= e(e_n + \beta), \quad n = 0, 1, 2 \ldots \end{aligned} \tag{4.11}$$

4.3 Solution of the Difference Equation

Our analysis requires the modulator state u_n, $n = 0, 1, 2, \ldots$ to be contained in the no-overload region R of the quantizer. R is the lightly shaded region of Fig. 4.1 consisting of the 7 hexagons closest to zero. S is the star-shaped shaded region of Fig. 4.1. The following sufficient condition for no-overload can be shown by induction: If $\beta \in S$ and $e_0 \in H$, then $e_n \in H$ and $u_n \in R$ for all $n = 0, 1, 2 \ldots$. We assume $\beta \in S$ and $e_0 \in H$ and hence no-overload for the rest of the paper.

Since the function $e(u) = u - q(u)$ coincides with $\bigcirc$ on the no-overload region R, the no-overload assumption implies that the difference equation (4.11) can be written as

$$e_{n+1} = \overline{\langle e_n + \beta \rangle} \tag{4.12}$$

Property (4.9) can be used to check that the solution to (4.12) is

$$e_n = \overline{\langle e_0 + n\beta \rangle} \tag{4.13}$$

4.4 Fourier and ergodic results

We state results about Fourier analysis and ergodic shifts. Let $f, g : \mathcal{P} \to \mathbb{C}$ be hexagonally periodic and Lebesgue square integrable on H. Then $f(x) = \sum_{p \in \Lambda^*} \hat{f}_p e^{i2\pi px}$ where the equality is interpreted in the L^2 sense and the Fourier coefficients are $\hat{f}_p = \frac{1}{|H|} \int_H f(s) e^{-i2\pi ps} ds$. Parseval's formula is

$$\frac{1}{|H|} \int_H f(s)\, g^*(s) ds = \sum_{p \in \Lambda^*} \hat{f}_p\, \hat{g}_p^* \tag{4.14}$$

These Fourier results can be obtained either as sketched in Appendix A or as a particular case of harmonic analysis on compact Abelian groups [52].

Identify points of $\mathcal{P}$ differing by vectors in Λ to define $\mathcal{H} = \mathcal{P}/\Lambda = \{x + \Lambda \mid x \in \mathcal{P}\}$. $\mathcal{H}$ is a compact Abelian group. A function $f : H \to \mathbb{C}$ *lifts* to a function $\tilde{f} : \mathcal{H} \to \mathbb{C}$ if $\tilde{f}(x + \Lambda) = f(x)$ for all x. Lemma 4.1 gives a generic condition on the input β for the dynamics (4.13) to induce a uniquely ergodic shift on $\mathcal{H}$ so that time averages of a function f can be evaluated as an integral over H:

Lemma 4.1 Let $\beta \in \mathcal{P}$ be such that the only $p \in \Lambda^*$ with $p\beta \in \mathbb{Z}$ is $p = 0$. Let $f : H \to \mathbb{R}$ have a continuous lifting $\tilde{f} : \mathcal{H} \to \mathbb{R}$. Then for all $e_0 \in \mathcal{P}$,

$$\lim_{L \to \infty} \frac{1}{L} \sum_{n=0}^{L-1} f(\overline{\langle e_0 + n\beta \rangle}) = \frac{1}{|H|} \int_H f(s) ds$$

Corollary 4.2 The result of Lemma 4.1 extends to functions $f : H \to \mathbb{R}$ for which there exist sequences of functions $\overline{f}_k$, $\underline{f}_k$, $k = 1, 2, \ldots$ with continuous liftings such that $\underline{f}_k(x) \leq f(x) \leq \overline{f}_k(x)$ for all x and $|\underline{f}_k - \overline{f}_k|_\infty \to 0$ as $k \to \infty$.

Lemma 4.1 can be obtained from standard results on the torus [53] as indicated in Appendix A.

4.5 Spectral Analysis

This section computes the power spectral density of the quantizer error function and the quantizer output for the hexagonal $\Sigma\Delta$ modulator with a constant input. There are three cases to consider, depending on the value of the constant input β. The three cases are characterized as follows.

Case 1: $\{s \in \Lambda^* \mid s\beta \in \mathbb{Z}\} = \{0\}$. In Case 1, the error sequence e_n described by (4.13) is equidistributed over H so that Lemma 4.1 applies. Case 1 is the generic case satisfied by $\beta \in H$ almost everywhere.

Case 2: $\{s \in \Lambda^* \mid s\beta \in \mathbb{Z}\} = \{mr \mid m \in \mathbb{Z}\}$ for some nonzero $r \in \Lambda^*$. Another characterization of Case 2 is that β has the form

$$\beta = \alpha r_\perp + \frac{z}{g}\sigma\,; \qquad r_\perp \in \Lambda, \sigma \in \Lambda, z \in \mathbb{Z}, g \in \mathbb{Z} \tag{4.15}$$

where $\alpha \in \mathbb{R}$ is irrational and $r_\perp \neq 0$. In Case 2, the sequence e_n described by (4.13) is confined to lines in H, but the sequence is aperiodic and equidistributed over the lines.

Case 3: β has the form

$$\beta = \frac{h}{q}v\,; \qquad v \in \Lambda, h \in \mathbb{Z}, q \in \mathbb{Z} \tag{4.16}$$

where h and q are relatively prime. In Case 3, the sequence e_n described by (4.13) is confined to discrete points in H and is periodic with period q.

Cases 1 - 3 and their characterizations are established in Appendix B.

4.6 Autocorrelation Computation

The autocorrelation matrix of the noise process is, using (4.13),

$$\begin{aligned} R_e(k) &= \lim_{L\to\infty} \frac{1}{L} \sum_{n=0}^{L-1} e_n \otimes e_{n+k} \\ &= \lim_{L\to\infty} \frac{1}{L} \sum_{n=0}^{L-1} \langle\!\langle e_0 + n\beta \rangle\!\rangle \otimes \langle\!\langle e_0 + n\beta + k\beta \rangle\!\rangle \end{aligned} \tag{4.17}$$

where $\otimes$ denotes outer product. The following three subsections compute the autocorrelation in Cases 1, 2 and 3 starting from (4.17).

4.6.1 Autocorrelation Computation Case 1

Case 1 is the generic case in which Lemma 4.1 applies and the calculation proceeds as a generalization of the method for the single-bit modulator presented in section 3.

Equation (4.17) may be modified using (4.9) to give

$$R_e(k) = \lim_{L\to\infty} \frac{1}{L} \sum_{n=0}^{L-1} \langle\!\langle e_0 + n\beta \rangle\!\rangle \otimes \langle\!\langle \langle\!\langle e_0 + n\beta \rangle\!\rangle + k\beta \rangle\!\rangle$$

Define $f : H \to \mathcal{P} \times \mathcal{P}$ by

$$f(s) = s \otimes \langle\!\langle s + k\beta \rangle\!\rangle \tag{4.18}$$

Then

$$R_e(k) = \lim_{L\to\infty} \frac{1}{L} \sum_{n=0}^{L-1} f\left(\langle\!\langle e_0 + n\beta \rangle\!\rangle\right)$$

Each component of f is continuous except on several line segments and satisfies the conditions of Corollary 4.2. Hence

$$R_e(k) = \frac{1}{|H|} \int_H \langle\!\langle s \rangle\!\rangle \otimes \langle\!\langle s + k\beta \rangle\!\rangle \, ds \tag{4.19}$$

Let c_p be the Fourier coefficients of $\langle\!\langle \bigcirc \rangle\!\rangle$ for $p \in \Lambda^*$:

$$c_p = \frac{1}{|H|} \int_H \langle\!\langle s \rangle\!\rangle \, e^{-i2\pi ps} ds \tag{4.20}$$

Appendix C computes c_p as

$$c_p = \frac{-i\,\mathrm{sgn}\,(p)\,p^t}{4\sqrt{3}\pi^2\Pi(p)} \tag{4.21}$$

where Π and sgn are defined as follows: Using coordinates (4.3) so that $p = (p_a, p_b, p_c)$, define $\Pi(p)$ = product of nonzero elements of $\{p_a, p_b, p_c\}$, $p \neq 0$ and $\Pi(0) = 1$. Partition $\Lambda^* = \Lambda^t \cup (n_a^t + \Lambda^t) \cup (-n_a^t + \Lambda^t)$ and define

$$\mathrm{sgn}\,(p) = \begin{cases} 0 & \text{if } p \in \Lambda^t, p_a p_b p_c \neq 0 \text{ or } p = 0, \\ 2\pi/\sqrt{3} & \text{if } p \in \Lambda^t, p_a p_b p_c = 0 \text{ and } p \neq 0, \\ 1 & \text{if } p \in n_a^t + \Lambda^t, \\ -1 & \text{if } p \in -n_a^t + \Lambda^t. \end{cases}$$

The Fourier coefficients of $f(x) = \overline{\langle x + k\beta \rangle}$ are $c_p\, e^{i2\pi p\beta k}$.

Each entry of the outer product in (4.19) can be regarded as an inner product of functions over H and applying Parseval's formula (4.14) to each entry gives

$$R_e(k) = \sum_{p \in \Lambda^*} c_p \otimes c_{-p}\, e^{-i2\pi p\beta k} \tag{4.22}$$

4.6.2 Autocorrelation Computation Case 2

Recall from (4.15) that in Case 2, $\beta = \alpha r_\perp + \frac{z}{g}\sigma$ where $r_\perp, \sigma \in \Lambda$ and $z, g \in \mathbb{Z}$ and $\alpha \in \mathbb{R}$ is irrational. Equation (4.17) for the autocorrelation matrix may be rewritten using (4.18) as

$$\begin{aligned} R_e(k) &= \lim_{L' \to \infty} \frac{1}{L'} \sum_{n=0}^{L'-1} f(\overline{\langle n\beta + e_0 \rangle}\,) \\ &= \lim_{L \to \infty} \frac{1}{gL} \sum_{n=0}^{L-1} \sum_{m=0}^{g-1} f(\overline{\langle (ng+m)\beta + e_0 \rangle}\,) \\ &= \frac{1}{g} \sum_{m=0}^{g-1} \lim_{L \to \infty} \frac{1}{L} \sum_{n=0}^{L-1} f(\overline{\langle \langle ng\alpha + m\alpha \rangle r_\perp + (mz/g)\sigma + e_0 \rangle}\,) \end{aligned}$$

Use α irrational and Weyl's ergodic theorem 3.1 to get

$$R_e(k) = \frac{1}{g}\sum_{m=0}^{g-1}\int_0^1 f(\langle\theta r_\perp + (mz/g)\sigma + e_0\rangle)d\theta$$
$$= \frac{1}{g}\sum_{m=0}^{g-1}\int_0^1 \langle\theta r_\perp + (mz/g)\sigma + e_0\rangle \otimes \langle\theta r_\perp + (mz/g)\sigma + k\beta + e_0\rangle\, d\theta \qquad (4.23)$$

The Fourier coefficients of the factors inside the integral in (4.23) can be obtained from their Fourier expansions:

$$\langle\theta r_\perp + (mz/g)\sigma + e_0\rangle = \sum_{p\in\Lambda^*} c_p e^{i2\pi(\theta p r_\perp + (mz/g)p\sigma + pe_0)}$$
$$= \sum_{n\in\mathbb{Z}}\sum_{\substack{p\in\Lambda^*\\ pr_\perp = n}} c_p e^{i2\pi((mz/g)p\sigma + pe_0)} e^{i2\pi n\theta}$$
$$\langle\theta r_\perp + (mz/g)\sigma + k\beta + e_0\rangle = \sum_{n\in\mathbb{Z}}\sum_{\substack{p'\in\Lambda^*\\ p'r_\perp = n}} c_{p'} e^{i2\pi((mz/g)p'\sigma + kp'\beta + p'e_0)} e^{i2\pi n\theta}$$

Applying Parseval's formula (3.14) to (4.23) gives

$$R_e(k) = \frac{1}{g}\sum_{m=0}^{g-1}\sum_{n\in\mathbb{Z}}\sum_{\substack{p\in\Lambda^*\\ pr_\perp = n}} c_p e^{i2\pi((mz/g)p\sigma + pe_0)} \otimes \sum_{\substack{p'\in\Lambda^*\\ p'r_\perp = n}} c^*_{p'} e^{-i2\pi((mz/g)p'\sigma + kp'\beta + p'e_0)} \qquad (4.24)$$

According to Appendix D, the summations in (4.24) are absolutely convergent and can be reordered to give

$$R_e(k) = \sum_{n\in\mathbb{Z}}\sum_{\substack{p,p'\in\Lambda^*\\ pr_\perp = n\\ p'r_\perp = n}} c_p \otimes c_{-p'} e^{-i2\pi kp'\beta}\frac{1}{g}\sum_{m=0}^{g-1} e^{i2\pi(mz/g)(p-p')\sigma} e^{i2\pi(p-p')e_0}$$
$$= \sum_{\substack{p,p'\in\Lambda^*\\ (p-p')r_\perp = 0\\ (p-p')\sigma = 0(\mathrm{mod}\ g)}} c_p \otimes c_{-p'} e^{-i2\pi kp'\beta} e^{i2\pi(p-p')e_0} \qquad (4.25)$$
$$= \sum_{\substack{p,p'\in\Lambda^*\\ (p-p')\beta\in\mathbb{Z}}} c_p \otimes c_{-p'} e^{-i2\pi kp'\beta} e^{i2\pi(p-p')e_0} \qquad (4.26)$$
$$= \sum_{\substack{p,s\in\Lambda^*\\ s\beta\in\mathbb{Z}}} c_p \otimes c_{s-p} e^{i2\pi kp\beta} e^{i2\pi se_0} \qquad (4.27)$$

The equivalence of (4.25) and (4.26) follows from (B.4) in Appendix B.

4.6.3 Autocorrelation Computation Case 3

Recall from (4.16) that in Case 3, $\beta = (h/q)\upsilon$ where $\upsilon \in \Lambda$ and $h, q \in \mathbb{Z}$ are relatively prime. Then (4.17) may be rewritten as

$$R_e(k) = \frac{1}{q}\sum_{m=0}^{q-1} \overline{\langle (m/q)\upsilon + e_0 \rangle} \otimes \langle (m/q)\upsilon + k\beta + e_0 \rangle \tag{4.28}$$

The Fourier coefficients of the factors inside the sum in (4.28) can be obtained from the Fourier expansions:

$$\begin{aligned}
\overline{\langle (m/q)\upsilon + e_0 \rangle} &= \sum_{p\in\Lambda^*} c_p e^{i2\pi((m/q)p\upsilon + pe_0)} \\
&= \sum_{n=0}^{q-1} \sum_{\substack{p\in\Lambda^* \\ p\upsilon = n (\mathrm{mod}\ q)}} c_p e^{i2\pi pe_0} e^{i2\pi nm/q}
\end{aligned}$$

$$\begin{aligned}
\langle (m/q)\upsilon + k\beta + e_0 \rangle &= \sum_{p\in\Lambda^*} c_p e^{i2\pi((m/q)p\upsilon + kp\beta + pe_0)} \\
&= \sum_{n=0}^{q-1} \sum_{\substack{p'\in\Lambda^* \\ p'\upsilon = n (\mathrm{mod}\ q)}} c_{p'} e^{i2\pi(kp'\beta + p'e_0)} e^{i2\pi nm/q}
\end{aligned}$$

Applying Parseval's formula for scalar discrete periodic functions to (4.28) gives

$$\begin{aligned}
R_e(k) &= \sum_{n=0}^{q-1} \sum_{\substack{p'\in\Lambda^* \\ p'\upsilon = n (\mathrm{mod}\ q)}} c_p e^{i2\pi pe_0} \otimes \sum_{\substack{p'\in\Lambda^* \\ p'\upsilon = n (\mathrm{mod}\ q)}} c^*_{p'} e^{-i2\pi(kp'\beta + p'e_0)} \\
&= \sum_{n=0}^{q-1} \sum_{\substack{p,p'\in\Lambda^* \\ p\upsilon = n (\mathrm{mod}\ q) \\ p'\upsilon = n (\mathrm{mod}\ q)}} c_p \otimes c_{-p'} e^{-i2\pi kp'\beta} e^{i2\pi(p-p')e_0} \\
&= \sum_{\substack{p,p'\in\Lambda^* \\ (p-p')\upsilon = 0 (\mathrm{mod}\ q)}} c_p \otimes c_{-p'} e^{-i2\pi kp'\beta} e^{i2\pi(p-p')e_0} \\
&= \sum_{\substack{p,p'\in\Lambda^* \\ (p-p')\beta\in\mathbb{Z}}} c_p \otimes c_{-p'} e^{-i2\pi kp'\beta} e^{i2\pi(p-p')e_0} \\
&= \sum_{\substack{p,s\in\Lambda^* \\ s\beta\in\mathbb{Z}}} c_p \otimes c_{s-p} e^{i2\pi kp\beta} e^{i2\pi se_0}
\end{aligned} \tag{4.29}$$

4.7 Formal Derivation of Autocorrelation in the Three Cases

As a supplement to the rigorous derivation above, we give a formal derivation of the autocorrelation that neglects issues of convergence and interchange of infinite operations. The purpose is to show the commonality between the three cases. Starting from (4.17),

$$\begin{aligned}
R_e(k) &= \lim_{L\to\infty} \frac{1}{L} \sum_{n=0}^{L-1} \overline{\langle n\beta + e_0 \rangle} \otimes \overline{\langle n\beta + k\beta + e_0 \rangle} \\
&= \lim_{L\to\infty} \frac{1}{L} \sum_{n=0}^{L-1} \sum_{p\in\Lambda^*} c_p e^{i2\pi(np\beta + pe_0)} \otimes \sum_{p'\in\Lambda^*} c_{p'} e^{i2\pi(np'\beta + kp'\beta + p'e_0)} \\
&= \sum_{p,p'\in\Lambda^*} c_p \otimes c_{p'} e^{i2\pi kp'\beta} e^{i2\pi(p+p')e_0} \lim_{L\to\infty} \frac{1}{L} \sum_{n=0}^{L-1} e^{i2\pi\theta(p+p')\beta} \\
&= \sum_{\substack{p,p'\in\Lambda^* \\ (p+p')\beta\in\mathbb{Z}}} c_p \otimes c_{p'} e^{i2\pi kp'\beta} e^{i2\pi(p+p')e_0} \\
&= \sum_{\substack{p,s\in\Lambda^* \\ s\beta\in\mathbb{Z}}} c_p \otimes c_{s-p} e^{-i2\pi kp\beta} e^{i2\pi se_0}
\end{aligned} \tag{4.30}$$

In Case 1, (4.30) reduces to the rigorously derived equation (4.22) since $s\beta \in \mathbb{Z}$ for $s \in \Lambda^*$ implies $s = 0$ in Case 1. Moreover, in Cases 2 and 3, (4.30) is the same as the rigorously derived equations (4.27) and (4.29).

4.8 Spectrum of Error and Output Sequence

According to (4.22), (4.27), and (4.29) for Cases 1, 2, and 3 the autocorrelation matrix may be rewritten in the general form

$$R_e(k) = \sum_{\substack{p,s\in\Lambda^* \\ s\beta\in\mathbb{Z}}} c_p \otimes c_{s-p}\, e^{i2\pi se_0}\, e^{-i2\pi p\beta k} \tag{4.31}$$

The absolute summability of the series (4.31) is proved in Appendix D and this implies uniform convergence of (4.31) with respect to k. Since almost periodic sequences are the uniform limit of trigonometric polynomials, we conclude that each matrix element of $R_e(k)$ is almost periodic [50].

Similarly to the scalar case, the Bohr-Fourier series (4.31) implies that the quantization error spectral matrix S_e is purely discrete having amplitudes $\sum_{\substack{s\in\Lambda^* \\ s\beta\in\mathbb{Z}}} c_p \otimes c_{s-p}\, e^{i2\pi s e_0}$ at frequencies $\langle p\beta\rangle$ for $p \in \Lambda^*$:

$$S_e(\omega) = \sum_{p\in\Lambda^*} \sum_{\substack{s\in\Lambda^* \\ s\beta\in\mathbb{Z}}} c_p \otimes c_{s-p}\, e^{i2\pi s e_0}\, \delta(\omega - \langle p\beta\rangle) \tag{4.32}$$

Note that the amplitudes are real because c_p and c_{s-p} are both imaginary (see (4.21)) so that $c_p \otimes c_{s-p}$ is real and because of the symmetry of the sum over s. In particular, $s\beta \in \mathbb{Z} \iff -s\beta \in \mathbb{Z}$.

The quantizer output q_n is obtained by differencing e_n and adding β according to (3.4). Hence the output spectral density matrix is

$$S_q(\omega) = \beta \otimes \beta\, \delta(\omega) + 4\sin^2(\pi\omega) S_e(\omega) \tag{4.33}$$

Now we examine some of the special forms of these spectra in the Cases 1, 2 and 3 described in section 4.5.

4.8.1 Spectra in Case 1

For generic input β satisfying Case 1, the error spectrum (4.32) reduces to

$$S_e(\omega) = \sum_{p\in\Lambda^*} c_p \otimes c_{-p}\, \delta(\omega - \langle p\beta\rangle) \tag{4.34}$$

and the output spectrum (4.33) becomes

$$S_q(\omega) = \beta \otimes \beta\, \delta(\omega) + \sum_{p\in\Lambda^*} \frac{\sin^2(\pi\omega)\mathrm{sgn}^2(p)}{12\pi^4 \Pi^2(p)}\, p \otimes p\, \delta(\omega - \langle p\beta\rangle) \tag{4.35}$$

Hence, the frequencies and therefore the amplitudes of the spectra depend strongly on the input β. Clearly the spectrum is far from white noise being neither white nor continuous.

4.8.2 Spectra in Case 2

Recall from (4.15) that in Case 2, $\beta = \alpha r_\perp + \frac{z}{g}\sigma$ where $r_\perp, \sigma \in \Lambda$ and $z, g \in \mathbb{Z}$ and $\alpha \in \mathbb{R}$ is irrational. Moreover $\{s \in \Lambda^* \mid s\beta \in \mathbb{Z}\} = \{mr \mid m \in \mathbb{Z}\}$. Then (4.32) can be written as

$$S_e(\omega) = \sum_{p\in\Lambda^*} \sum_{m\in\mathbb{Z}} c_p \otimes c_{mr-p}\, e^{i2\pi m r e_0}\, \delta\left(\omega - \left\langle \alpha p r_\perp + \frac{z}{g} p\sigma \right\rangle\right) \tag{4.36}$$

4.8.3 Spectra in Case 3

Recall from (4.16) that in Case 3, $\beta = (h/q)v$ where $v \in \Lambda$ and $h, q \in \mathbb{Z}$. Then (4.32) can be written as

$$S_e(\omega) = \sum_n \sum_{\substack{p,s\in\Lambda^* \\ pv=n(\mathrm{mod}\ q) \\ sv=0(\mathrm{mod}\ q)}} c_p \otimes c_{s-p}\, e^{i2\pi s e_0}\, \delta\left(\omega - \left\langle \frac{hn}{q} \right\rangle\right) \tag{4.37}$$

showing that frequencies are equally spaced at multiples of $1/q$. The output spectrum frequencies are spaced in the same way.

4.9 Mean and Variance

This section computes the mean and variance of the quantizer error function for the hexagonal $\Sigma\Delta$ modulator in Case 1 of a generic constant input.

The mean of the noise process is, using (4.13),

$$\overline{e} = \lim_{L\to\infty} \frac{1}{L} \sum_{n=0}^{L-1} e_n = \lim_{L\to\infty} \frac{1}{L} \sum_{n=0}^{L-1} \overline{\langle e_0 + n\beta \rangle}\ . \tag{4.38}$$

Applying Lemma 4.1 to (4.38) yields

$$\overline{e} = \frac{1}{|H|} \int_H s\, ds = 0. \tag{4.39}$$

The quantizer output q is obtained by differencing e and adding β according to (3.4). Hence, as expected, the mean quantizer output is $\overline{q} = \beta$.

The covariance matrix σ_e^2 of the quantizer error is $R_e(0)$, the autocorrelation matrix evaluated at zero. Calculation of $R_e(0)$ from (4.19) is straightforward [14]:

$$\sigma_e^2 = \frac{1}{|H|} \int_H s \otimes s\, ds = \frac{5}{36}\frac{1}{3} \begin{bmatrix} 2 & -1 & -1 \\ -1 & 2 & -1 \\ -1 & -1 & 2 \end{bmatrix}. \tag{4.40}$$

Hence the variance of one component of e is $10/108 = 0.0926$.

Chapter 5

Autocorrelation Calculation

This chapter computes a closed form formula for the autocorrelation of the hexagonal $\Sigma\Delta$ modulator assuming a generic constant input. Detailed analytic proof of the calculation steps has not been attempted; delta functions are used freely in integrands and various smoothness assumptions are asserted. The places in which these assumptions are made are noted. The notation used in this chapter is given in Section 4.1. The closed form autocorrelation formula is numerically validated against the rigorous result of Chapter 4.

The autocorrelation function of the hexagonal $\Sigma\Delta$ modulator is

$$R_e(y) = \frac{1}{|H|}\int_H \langle\!\langle s+y \rangle\!\rangle \otimes s \, ds \tag{5.1}$$

Since $s \mapsto \langle\!\langle s+y \rangle\!\rangle$ is piecewise linear with discontinuities only along a finite number of line segments in H, R_e is continuous. We first choose y in the interior of a particular hexagon sextant and later vary the sextant and then extend R_e to H by continuity.

Choose y in the interior of a particular hexagon sextant. Define $f : [0,1] \to \mathcal{P}^2$ by

$$f(\alpha) = R_e(\alpha y) \tag{5.2}$$

This definition ensures that $f(\alpha)$ lies within the interior of the sextant containing y except that $f(0) = 0$. The strategy to evaluate $R_e(y) = f(1)$ is to expand f in a Taylor series about zero.

5.0.1 Constant Term

Calculation of $R_e(0)$ is straightforward [14].

$$f(0) = R_e(0) = \frac{1}{|H|}\int_H \langle\!\langle s \rangle\!\rangle \otimes s \, ds = \frac{5}{36}P \tag{5.3}$$

5.0.2 Linear Term

In the following we allow delta functions in the integrand. Assuming that f is differentiable and that we can interchange differentiation and integration,

$$\nabla_\alpha f = \frac{1}{|H|}\int_H \nabla_\alpha \langle\!\langle s+\alpha y \rangle\!\rangle \otimes s\, ds \tag{5.4}$$

Since $D_x \langle\!\langle x+y \rangle\!\rangle = D_y \langle\!\langle x+y \rangle\!\rangle$,

$$\nabla_\alpha f = \frac{1}{|H|}\int_H \nabla_s \left(\langle\!\langle s+\alpha y \rangle\!\rangle \cdot y\right) \otimes s\, ds \tag{5.5}$$

By the product rule,

$$\begin{aligned}\nabla_\alpha f =& \frac{1}{|H|}\int_H \nabla_s(\langle\!\langle s+\alpha y \rangle\!\rangle \cdot y\, s)ds - \frac{1}{|H|}\int_H \langle\!\langle s+\alpha y \rangle\!\rangle \cdot y\, ds \otimes I \\ =& \frac{1}{|H|}\int_H \nabla_s(\langle\!\langle s+\alpha y \rangle\!\rangle \cdot y\, s)ds \end{aligned} \tag{5.6}$$

Applying Stokes theorem as developed in Section 5.2, we obtain an integral along the hexagon sides with respect to arc length ℓ.

$$\nabla_\alpha f = \frac{1}{|n^\perp||H|}\oint_{\partial H} \langle\!\langle \ell+\alpha y \rangle\!\rangle \cdot y\, \ell \otimes n_\ell^\perp d\ell \tag{5.7}$$

Let a, b, c be any three non-opposite hexagon sides. Then

$$\begin{aligned}\nabla_\alpha f =& \frac{1}{|n^\perp||H|}\sum_{s\in\{a,b,c\}}\int_{\partial H_s} \langle\!\langle \ell+\alpha y \rangle\!\rangle \cdot y\, \ell \otimes n_\ell^\perp + \langle\!\langle \ell - n_\ell^\perp + \alpha y \rangle\!\rangle \cdot y\,(\ell - n_\ell^\perp) \otimes (-n_\ell^\perp) d\ell \\ =& \frac{1}{|n^\perp||H|}\sum_{s\in\{a,b,c\}}\int_{\partial H_s} \langle\!\langle \ell+\alpha y \rangle\!\rangle \cdot y\, d\ell\, n_s^\perp \otimes n_s^\perp \end{aligned} \tag{5.8}$$

Since

$$\lim_{\substack{\alpha\to 0\\ \alpha>0}} \langle\!\langle \ell+\alpha y \rangle\!\rangle = \ell - \frac{1}{2}\left(1+\operatorname{sgn}(y_\ell^\perp)\right) n_\ell^\perp$$

we have by interchanging limit and integral

$$\begin{aligned}
\nabla_\alpha f|_0 &= \lim_{\substack{\alpha\to 0\\ \alpha>0}} \nabla_\alpha f \\
&= \frac{1}{|n^\perp||H|}\sum_{s\in\{a,b,c\}}\int_{\partial H_s}\left(\ell - \frac{1}{2}\left(1+\operatorname{sgn}\left(y_\ell^\perp\right)\right)n_\ell^\perp\right)\cdot y\, d\ell\, n_s^\perp\otimes n_s^\perp \\
&= \frac{1}{|n^\perp||H|}\sum_{s\in\{a,b,c\}}\left[\int_{\partial H_s}\left(\ell-\frac{1}{2}n_s^\perp\right)d\ell\cdot y - \frac{1}{2}|n|\,|y_s^\perp|\right]n_s^\perp\otimes n_s^\perp \\
&= \frac{-|n|}{2|n^\perp||H|}\sum_{s\in\{a,b,c\}}|y_s^\perp|\,n_s^\perp\otimes n_s^\perp \\
&= -\frac{1}{6}\sum_{s\in\{a,b,c\}}|y_s^\perp|\,n_s^\perp\otimes n_s^\perp
\end{aligned} \tag{5.9}$$

using $|H|=\sqrt{3}$, $|n^\perp|=\sqrt{2}$, and $|n|=\sqrt{2/3}$.

5.0.3 Quadratic Term

Calculate $\nabla_{\alpha\alpha}f$ by differentiating (5.8). Let a,b,c be any three non-opposite hexagon sides and simplify similarly to the linear term:

$$\begin{aligned}
\nabla_{\alpha\alpha}f =& \frac{1}{|n^\perp||H|}\sum_{s\in\{a,b,c\}}\int_{\partial H_s}\nabla_\alpha\overbrace{\langle \ell+\alpha y\rangle}\cdot y\, d\ell\, n_s^\perp\otimes n_s^\perp \\
=& \frac{1}{|n^\perp||H|}\sum_{s\in\{a,b,c\}}\int_{\partial H_s}(\nabla_\ell\overbrace{\langle \ell+\alpha y\rangle}\cdot y)\cdot y\, d\ell\, n_s^\perp\otimes n_s^\perp \\
=& \frac{1}{|n^\perp||H|}\sum_{s\in\{a,b,c\}}\left[|n||y|^2 - \int_{\partial H_s}(\nabla_\ell q(\ell+\alpha y)\cdot y)\cdot y\, d\ell\right]n_s^\perp\otimes n_s^\perp \\
=& \frac{3|n||y|^2}{|n^\perp||H|}P - \frac{1}{|n^\perp||H|}\sum_{s\in\{a,b,c\}}\left[\int_{\partial H_s}(\nabla_\ell q(\ell+\alpha y)\cdot y)\cdot y\, d\ell\right]n_s^\perp\otimes n_s^\perp
\end{aligned} \tag{5.10}$$

since $\sum_{s\in\{a,b,c\}} n_s^\perp\otimes n_s^\perp = 3P$. We claim that

$$\nabla_\ell q(\ell) = \delta\left(|\overbrace{\langle\ell\rangle}|_1 - \frac{|n^\perp|_1}{2}\right)n_\ell^\perp\otimes n_\ell^\perp \tag{5.11}$$

Substituting for $\nabla_\ell q$ in (5.10) gives

$$\nabla_{\alpha\alpha}f = |y|^2 P - \frac{1}{\sqrt{6}}\sum_{s\in\{a,b,c\}}\int_{\partial H_s}\delta\left(|\overbrace{\langle\ell+\alpha y\rangle}|_1 - 1\right)(n_{\ell+\alpha y}^\perp\cdot y)^2 d\ell\, n_s^\perp\otimes n_s^\perp \tag{5.12}$$

See Fig. 5.1 for an illustration of the second term of $\nabla_{\alpha\alpha} f$.

By employing the ordered coordinate system developed in Section 4.1, the integral in (5.12) vanishes for $s = 1$, becomes $|n|(y_3^{\perp})^2$ for $s = 2$, and becomes $|n|(y_2^{\perp})^2$ for $s = 3$. Thus

$$\nabla_{\alpha\alpha} f = |y|^2 P - \frac{1}{3}\left[n_3^{\perp} \otimes n_3^{\perp}(y_2^{\perp})^2 + n_2^{\perp} \otimes n_2^{\perp}(y_3^{\perp})^2\right] \tag{5.13}$$

It is now clear that $\nabla_{\alpha\alpha} f$ is a constant with respect to α. Therefore the Taylor series for f only includes constant, linear and quadratic terms:

$$\begin{aligned} R_e(y) &= f(1) = f(0) + \nabla_{\alpha} f|_0 + \frac{1}{2}\nabla_{\alpha\alpha} f \\ &= \left(\frac{5}{36} + \frac{|y|^2}{2}\right) P - \frac{1}{6} \sum_{s\in\{a,b,c\}} |y_s^{\perp}|\, n_s^{\perp} \otimes n_s^{\perp} - \frac{1}{6}\left[n_3^{\perp} \otimes n_3^{\perp}(y_2^{\perp})^2 + n_2^{\perp} \otimes n_2^{\perp}(y_3^{\perp})^2\right] \end{aligned} \tag{5.14}$$

Thus formula (5.14) depends on which sextant y is in.

The derivation assumes that y is in the interior of its sextant. Since $R_e(y)$ is continuous on H, the value of $R_e(y)$ on the sextant borders can be obtained as a limiting case of formula (5.14). For clarity, we consider the border between sextant a and sextant $-b$. This border lies along n_c. In sextant a, the third term of (5.14) is

$$-\frac{1}{6}\left[n_b^{\perp} \otimes n_b^{\perp}(y_c^{\perp})^2 + n_c^{\perp} \otimes n_c^{\perp}(y_b^{\perp})^2\right]$$

and this tends to

$$-\frac{1}{6}\left[n_c^{\perp} \otimes n_c^{\perp}(y_b^{\perp})^2\right] \tag{5.15}$$

as y tends to the border within sextant a. In sextant $-b$, the third term of (5.14) is

$$-\frac{1}{6}\left[n_c^{\perp} \otimes n_c^{\perp}(y_a^{\perp})^2 + n_a^{\perp} \otimes n_a^{\perp}(y_c^{\perp})^2\right]$$

and this tends to

$$-\frac{1}{6}\left[n_c^{\perp} \otimes n_c^{\perp}(y_a^{\perp})^2\right] \tag{5.16}$$

as y tends to the border. But on the border, $(y_b^{\perp})^2 = (y_a^{\perp})^2$ so that expressions (5.15) and (5.16) coincide.

However, the derivative of $R_e(y)$ is not continuous at the sextant borders. Thus $R_e(y)$ is quadratic within sextants but merely continuous at sextant borders; in short, $R_e(y)$ is piecewise quadratic.

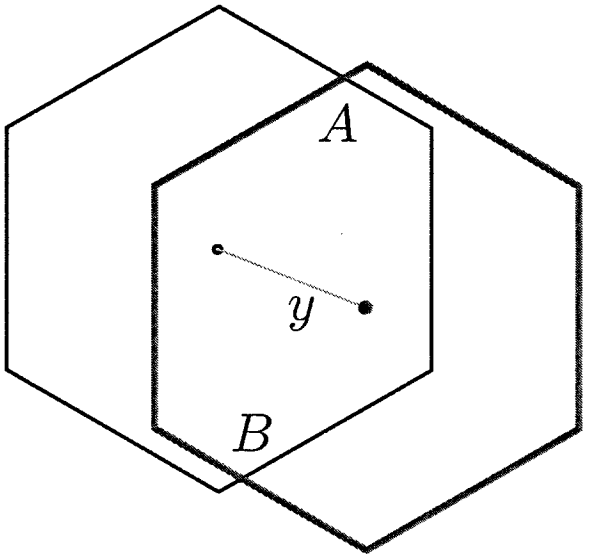

Figure 5.1 Illustration of second term of $\nabla_{\alpha\alpha} f$.

5.1 Numerical Verification of the Autocorrelation Formula

We present a numerical check through MATHEMATICA of the autocorrelation formula, (5.14) by comparing it to the rigorously derived series (4.22).

For the input $\beta = (0.0298658, 0.188285, -0.218151)$, formula (5.14) produces the following autocorrelation matrix

$$\begin{pmatrix} 0.03839617 & -0.02362990 & -0.01476626 \\ -0.02362990 & 0.01617576 & 0.00745414 \\ -0.01476626 & 0.00745414 & 0.00731212 \end{pmatrix}$$

Computation of the summation (4.22) over 7650 terms of Λ^*

$$\begin{pmatrix} 0.03838994 & -0.02362614 & -0.01476379 \\ -0.02362614 & 0.01617260 & 0.00745353 \\ -0.01476379 & 0.00745353 & 0.00731026 \end{pmatrix}$$

resulting in an error of

$$\begin{pmatrix} -6.2 \times 10^{-6} & 3.7 \times 10^{-6} & 2.4 \times 10^{-6} \\ 3.7 \times 10^{-6} & -3.1 \times 10^{-6} & -6.0 \times 10^{-7} \\ 2.4 \times 10^{-6} & -6.0 \times 10^{-7} & -1.8 \times 10^{-6} \end{pmatrix}$$

5.2 Line Integrals, Differential Forms, and Stokes Theorem

In this section, we specialize Stokes theorem to the case of a scalar function on the hexagon H. Stokes theorem allows us to rewrite area integrals on H as line integrals on the boundary of the hexagon, ∂H. Much of the terminology and notation is copied from Spivak [54].

Regard the hexagon H as a singular 2-cube $H : [0,1]^2 \to \mathbb{R}^2$. Then the boundary ∂H is a 1-chain which is the sum of the sides, each with the orientation given by a counterclockwise motion around H. Let ϕ be a smooth real function on $\mathbb{R}^2$.

Define the vector 1-form

$$\omega = \phi \begin{bmatrix} dy \\ -dx \end{bmatrix} \tag{5.17}$$

Then

$$d\omega = \begin{bmatrix} d\phi \wedge dy \\ -d\phi \wedge dx \end{bmatrix} = \begin{bmatrix} \frac{\partial \phi}{\partial x} \\ \frac{\partial \phi}{\partial y} \end{bmatrix} dx \wedge dy = \nabla \phi \; dx \wedge dy \tag{5.18}$$

Stokes theorem

$$\int_H d\omega = \int_{\partial H} \omega \tag{5.19}$$

becomes

$$\int_H \nabla \phi \; dx \wedge dy = \int_{\partial H} \phi \begin{bmatrix} dy \\ -dx \end{bmatrix} \tag{5.20}$$

Now we change coordinates on the right hand side of (5.20) from xy coordinates to $\ell\psi$ coordinates where ℓ is arc length along a given curve and ψ is the angle between curve tangent and the x axis. The coordinates are related by

$$\begin{aligned} x &= \ell\cos\psi + x_0 \\ y &= \ell\sin\psi + y_0 \end{aligned} \tag{5.21}$$

where x_0, y_0 is the point on the curve corresponding to $\ell = 0$. Now

$$\begin{aligned} dx &= \cos\psi\, d\ell - \ell\sin\psi\, d\psi \\ dy &= \sin\psi\, d\ell + \ell\cos\psi\, d\psi \end{aligned} \tag{5.22}$$

The right hand side of (5.20) becomes

$$\int_{\partial H} \phi \begin{bmatrix} \sin\psi \\ -\cos\psi \end{bmatrix} d\ell + \int_{\partial H} \phi\ell \begin{bmatrix} \cos\psi \\ \sin\psi \end{bmatrix} d\psi \tag{5.23}$$

But the second integral of (5.23) vanishes since ψ is constant along hexagon sides. Hence

$$\int_H \nabla\phi\ dx \wedge dy = \frac{1}{|n_\ell|}\int_{\partial H} \phi\, n_\ell\, d\ell \tag{5.24}$$

where

$$\frac{n_\ell}{|n_\ell|} = \begin{bmatrix} \sin\psi \\ -\cos\psi \end{bmatrix}$$

is the unit vector normal to the hexagon side.

Result (5.24) is developed under the assumption that ϕ is smooth, however it can be extended to functions with step discontinuities.

Chapter 6

Average Switching Rate

Switching rate is an important performance measure in power electronic systems since device switching loss is directly proportional to the switching rate. After deriving the average switching rates for the single-bit and hexagonal $\Sigma\Delta$ modulators, we proceed to determine the switching rate for slowly varying sinusoidal inputs.

6.1 Single-Bit $\Sigma\Delta$ Modulator

We derive the average switching rate for the single-bit $\Sigma\Delta$ modulator with the assumptions of no-overload and constant irrational input β.

First use (3.4) and notation from section 3.2 to show that

$$\begin{aligned} q_{n+1} - q_n &= -e_{n+1} + 2e_n - e_{n-1} \\ &= -\langle e_n + \beta \rangle + 2e_n - \langle e_n - \beta \rangle \\ &= \lfloor e_n + \beta \rfloor + \lfloor e_n - \beta \rfloor \end{aligned}$$

The precise condition for no switching between n and $n+1$ is

$$q_{n+1} = q_n \iff \lfloor e_n + \langle \beta \rangle \rfloor + \lfloor e_n - \langle \beta \rangle \rfloor = 0$$

Write χ for the indicator function, so that the average switching rate f_s is given by

$$\begin{aligned} 1 - f_s &= \lim_{L\to\infty} \frac{1}{L} \sum_{n=0}^{L-1} \chi\,[\text{no switching between } n,\, n+1] \\ &= \lim_{L\to\infty} \frac{1}{L} \sum_{n=0}^{L-1} \chi\,[\,|\lfloor e_n + \beta \rfloor + \lfloor e_n - \beta \rfloor| = 0\,] \\ &= \int_0^1 \chi\,[\,|\lfloor s + \beta \rfloor + \lfloor s - \beta \rfloor| = 0\,]\, ds \end{aligned} \tag{6.1}$$

by Theorem 3.1. By inspection (6.1) is

$$f_s = \begin{cases} 2\beta, & 0 \le \beta < 1/2, \\ 2(1-\beta), & 1/2 \le \beta < 1. \end{cases} \tag{6.2}$$

The maximum switching rate $f_s = 1$ occurs at $\beta = 1/2$.

6.2 Hexagonal $\Sigma\Delta$ Modulator

We derive the switching rate for the hexagonal $\Sigma\Delta$ modulator with constant input vector $\beta \in S$ (see Fig. 4.1). No-overload and generic β satisfying Case 1 are assumed.

First use (3.4), (4.9) and the definition of q in section 4.2 to show that

$$\begin{aligned} q_{n+1} - q_n &= -e_{n+1} + 2e_n - e_{n-1} \\ &= -\langle e_n + \langle\!\langle \beta \rangle\!\rangle \rangle + 2e_n - \langle e_n - \langle\!\langle \beta \rangle\!\rangle \rangle \\ &= q(e_n + \langle\!\langle \beta \rangle\!\rangle\,) + q(e_n - \langle\!\langle \beta \rangle\!\rangle\,). \end{aligned}$$

The precise condition for no switching between n and $n+1$ is

$$\begin{aligned} q_{n+1} = q_n &\iff q(e_n + \langle\!\langle \beta \rangle\!\rangle\,) + q(e_n - \langle\!\langle \beta \rangle\!\rangle\,) = 0 \\ &\iff q(e_n + \langle\!\langle \beta \rangle\!\rangle\,) = 0 \quad \text{and} \quad q(e_n - \langle\!\langle \beta \rangle\!\rangle\,) = 0 \end{aligned} \tag{6.3}$$

since $0 \neq q(e_n + \langle\!\langle \beta \rangle\!\rangle\,) = -q(e_n - \langle\!\langle \beta \rangle\!\rangle\,)$ is impossible. Write $H + \langle\!\langle \beta \rangle\!\rangle$ for the hexagon H translated by $\langle\!\langle \beta \rangle\!\rangle$ so that (6.3) may be written as $e_n \in H - \langle\!\langle \beta \rangle\!\rangle$ and $e_n \in H + \langle\!\langle \beta \rangle\!\rangle$. Then the precise condition for no switching between n and $n+1$ is

$$e_n \in (H - \langle\!\langle \beta \rangle\!\rangle\,) \cap (H + \langle\!\langle \beta \rangle\!\rangle\,) \tag{6.4}$$

Using Corollary 4.2 the average switching rate f_s is given by

$$\begin{aligned} 1 - f_s &= \lim_{L\to\infty} \frac{1}{L} \sum_{n=0}^{L-1} \chi\left[\text{no switching between } n,\, n+1\right] \\ &= \lim_{L\to\infty} \frac{1}{L} \sum_{n=0}^{L-1} \chi\left[e_n \in (H - \langle\!\langle \beta \rangle\!\rangle) \cap (H + \langle\!\langle \beta \rangle\!\rangle)\right] \\ &= \frac{1}{|H|} \int_H \chi\left[s \in (H - \langle\!\langle \beta \rangle\!\rangle) \cap (H + \langle\!\langle \beta \rangle\!\rangle)\right] ds \\ &= \frac{1}{|H|} \text{Area}\left[(H - \langle\!\langle \beta \rangle\!\rangle) \cap (H + \langle\!\langle \beta \rangle\!\rangle)\right] \end{aligned} \tag{6.5}$$

Equation (6.5) relates f_s to the overlapping area of two shifted hexagons as shown in Figs. 6.1 and 6.2. This is a useful geometric interpretation. For instance, we immediately see that f_s is maximum for β on the perimeter of H. To compute the area (6.5) for $\beta \in S$, there are three cases:

Case A: $\beta \in U^c \cap H$. Consider the particular case of β in the lower half of the $n_b^\perp$ sextant as shown in Fig. 6.1. According to (6.5), the switching rate is

$$f_s = 1 - \frac{1}{|H|} \text{Area}(ABDC) = 1 - \frac{\sqrt{3}}{2|H|} |AB|\, |BD| \tag{6.6}$$

By computing the positions of A, B, D in terms of the vertices of H and β, it can be shown that $|AB| = -2(\beta_b^\perp - 1)|n|$ and $|BD| = 2(\beta_c^\perp + 1)|n|$. Hence

$$\begin{aligned} f_s &= 1 + \frac{4}{3}(\beta_b^\perp - 1)(\beta_c^\perp + 1) \\ &= -\frac{1}{3} + \frac{4}{3}(|\beta_b^\perp| + |\beta_c^\perp| - |\beta_b^\perp||\beta_c^\perp|) \end{aligned}$$

Using the ordered coordinates described in section 4, the general case for any $\beta \in U^c \cap H$ is

$$f_s = -\frac{1}{3} + \frac{4}{3}\left(|\beta_1^\perp| + |\beta_2^\perp| - |\beta_1^\perp||\beta_2^\perp|\right) \tag{6.7}$$

Case B: $\beta \in U$. Consider the particular case of β in the lower half of the $n_b^\perp$ sextant as shown in Fig. 6.2. The switching rate is:

$$\begin{aligned} f_s &= 1 - \frac{1}{|H|} \text{Area}(ABPDCQ) \\ &= 1 - \frac{1}{|H|}\left(|BP||BQ| + \frac{\sqrt{3}}{2}|AB||AQ|\right) \end{aligned}$$

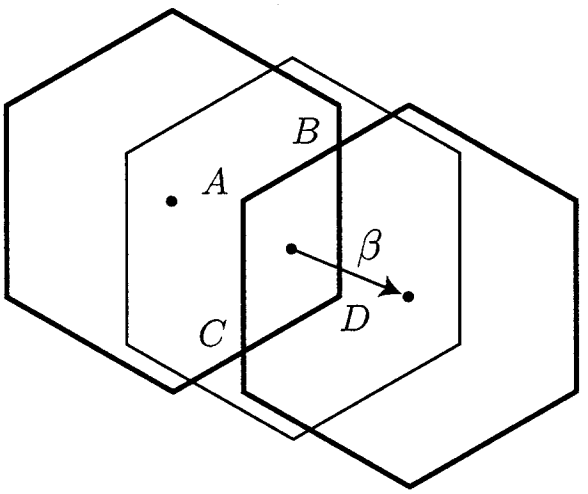

Figure 6.1 Overlap of 2 shifted hexagons for $\beta \in U^c \cap H$.

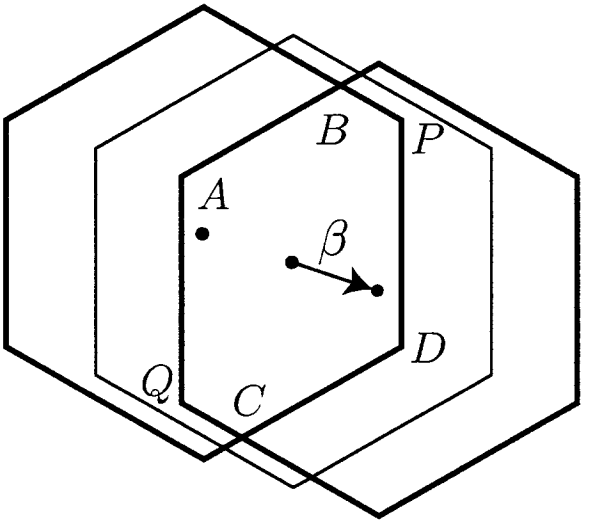

Figure 6.2 Overlap of 2 shifted hexagons for $\beta \in U$.

By computing the positions of A, B, P, Q, it can be shown that $|BP| = |n|(2\beta_c^{\perp} + 1)$, $|BQ| = |n^{\perp}|(\beta_a^{\perp} + 1)$, $|AB| = |n|(2\beta_a^{\perp} + 1)$, and $|AQ| = |n|$. Hence

$$f_s = -\frac{4}{3}\left(\beta_c^{\perp} + \beta_a^{\perp} + \beta_c^{\perp}\beta_a^{\perp}\right) = \frac{4}{3}\left(|\beta_c^{\perp}| + |\beta_a^{\perp}| - |\beta_c^{\perp}\beta_a^{\perp}|\right)$$

The general case for any $\beta \in U$ is, using (4.4),

$$f_s = \frac{4}{3}\left(|\beta_2^{\perp}| + |\beta_3^{\perp}| - |\beta_2^{\perp}||\beta_3^{\perp}|\right) = \frac{4}{3}\left(|\beta_1^{\perp}| - |\beta_2^{\perp}||\beta_3^{\perp}|\right) \tag{6.8}$$

Case C: $\beta \in H^c \cap S$. Since (6.5) is a function of $\langle\!\langle \beta \rangle\!\rangle$, the average switching rate at $\beta \in H^c \cap S$ is equal to the average switching rate at $\langle\!\langle \beta \rangle\!\rangle = \beta - q(\beta) \in H$.

Fig. 6.3 shows a contour plot of the switching rate evaluated with (6.7) and (6.8). The switching rate is zero at the origin and has its maximum value of one on the perimeter of H. For small β the product term in (6.8) is negligible and hence the contours are approximately hexagonal near the origin.

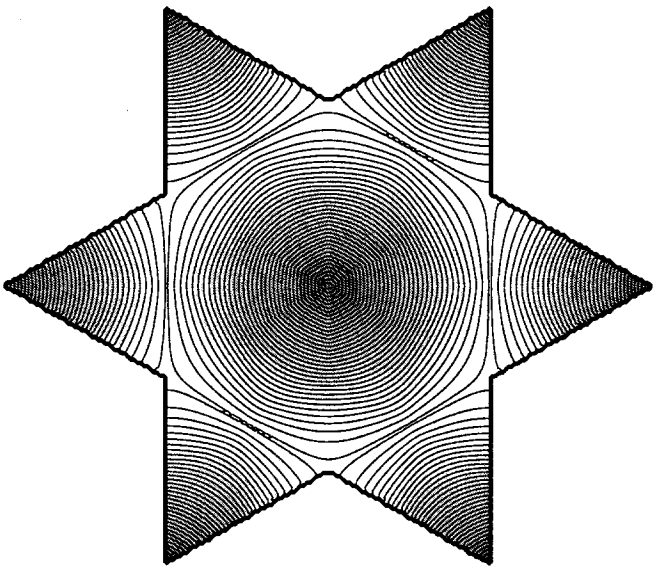

Figure 6.3 Switching rate contour plot over region S.

6.3 Slowly Varying Sinusoidal Inputs

Up to this point we have only considered dc inputs. However, in practice one is usually interested in the behavior of the modulator under sinusoidal inputs since power electronic systems typically generate variable amplitude, variable frequency sinusoidal waves to drive an induction machine.

We determine the switching rate for sinusoidal inputs that are slowly varying with respect to the switching rate. Sinusoidal inputs correspond to circles in the plane $\mathcal{P}$ and the circle radius is proportional to the sinusoidal input amplitude. This section computes the average switching rate on circles as the radius is varied, and then quantifies the deviations of the switching rate from the average switching rate as the circle is traversed.

To describe the circles it is convenient to use polar coordinates (r, θ) in the plane $\mathcal{P}$. The transformation to coordinates (4.2) is

$$\begin{pmatrix} \beta_a^\perp \\ \beta_b^\perp \\ \beta_c^\perp \end{pmatrix} = \begin{bmatrix} -1 & \sqrt{3} \\ 2 & 0 \\ -1 & -\sqrt{3} \end{bmatrix} \begin{pmatrix} r\cos\theta \\ r\sin\theta \end{pmatrix} \tag{6.9}$$

For example, $n_b^\perp$ has polar coordinates $(r, \theta) = (1, 0)$.

Formulas (6.8) and (6.7) for the switching rate f_s have a 12-fold symmetry in β (f_s is unchanged by reflection in the axes of symmetry along $n_a^\perp, n_b^\perp, n_c^\perp, n_a, n_b, n_c$). Therefore, the average switching rate $\hat{f}_s(r)$ on a circle of radius r can be computed on a sector of the circle such as $\theta \in [0, \pi/6]$:

$$\hat{f}_s(r) = \frac{6}{\pi} \int_0^{\pi/6} f_s(r, \theta)\, d\theta \tag{6.10}$$

To evaluate (6.10), there are three cases according to how the sector of the circle intersects the regions U, H, and S.

Case A: $0 \le r \le \sqrt{3}/6$. The sector of the circle lies inside U and the switching rate formula (6.8) specializes to

$$f_s = \frac{4}{3}\left(\beta_b^\perp - \beta_a^\perp \beta_c^\perp\right) = \frac{8}{3} r\cos\theta + \frac{4}{3} r^2 \left(1 - 2\cos 2\theta\right) \tag{6.11}$$

Evaluating (6.10) using (6.11) gives

$$\hat{f}_s = \frac{8}{\pi} r - \frac{4}{\pi}\left(\sqrt{3} - \frac{\pi}{3}\right) r^2, \qquad 0 \le r \le \sqrt{3}/6. \tag{6.12}$$

Case B: $\sqrt{3}/6 < r \le 1/2$. The sector of the circle lies in U for $\theta \in [0, \theta_1]$ and in $H \cap U^c$ for $\theta \in (\theta_1, \pi/6]$. The boundary of U satisfies $|\beta_2^\perp| = |\beta_a^\perp| = 1/2$. (4.8) and (6.9) yields

$$\theta_1 = \sec^{-1} \frac{8r}{1 + \sqrt{48r^2 - 3}} \tag{6.13}$$

In $H \cap U^c$ switching rate formula (6.7) specializes to

$$\begin{aligned} f_s &= -\frac{1}{3} + \frac{4}{3}\left(\beta_b^\perp - \beta_a^\perp + \beta_b^\perp \beta_a^\perp\right) \\ &= -\frac{1}{3} + \frac{4}{3} r \left(3\cos\theta + \sqrt{3}\sin\theta\right) - \frac{8}{3} r^2 \left(\cos^2\theta + \sqrt{3}\cos\theta\sin\theta\right) \end{aligned} \tag{6.14}$$

Evaluating (6.10) using (6.11) for $\theta \in [0, \theta_1]$ and (6.14) for $\theta \in (\theta_1, \pi/6]$ gives

$$\hat{f}_s = \frac{2}{\pi}\theta_1 - \frac{1}{3} + \frac{16}{\pi} r \cos(\theta_1 + \frac{\pi}{6}) + 4r^2 \left(\frac{4}{\pi}\theta_1 - \frac{1}{3} - \frac{2}{\pi}\cos(2\theta_1 - \frac{\pi}{6})\right), \qquad \sqrt{3}/6 < r \le 1/2. \tag{6.15}$$

Case C: $1/2 < r \le 1/\sqrt{3}$. As shown in Fig. 6.4, the sector of the circle lies in $S \cap H^c$ for $\theta \in [0, \theta_2]$ and in $H \cap U^c$ for $\theta \in (\theta_2, \pi/6]$ where

$$\theta_2 = \sec^{-1} 2r \tag{6.16}$$

The switching rate for the sector of the circle in $S \cap H^c$ for $\theta \in [0, \theta_2]$ is equal to the switching rate for the reflection of this sector in the edge of the hexagon H. (The reflected sector may be obtained by mapping the sector inside H using $\langle\rangle$ and then reflecting in a vertical axis. According to (6.5) and the 12-fold symmetry of (6.8) and (6.7), these operations preserve the switching rate). The reflected sector is a sector of the circle of radius r centered on $n_b^\perp$ and may be parameterized by $\theta \in [0, \theta_2]$ as $(1 - r\cos\theta, r\sin\theta)^t$ in rectangular coordinates and as

$$\begin{pmatrix} \beta_a^\perp \\ \beta_b^\perp \\ \beta_c^\perp \end{pmatrix} = \begin{bmatrix} -1 & \sqrt{3} \\ 2 & 0 \\ -1 & -\sqrt{3} \end{bmatrix} \begin{pmatrix} 1 - r\cos\theta \\ r\sin\theta \end{pmatrix} \tag{6.17}$$

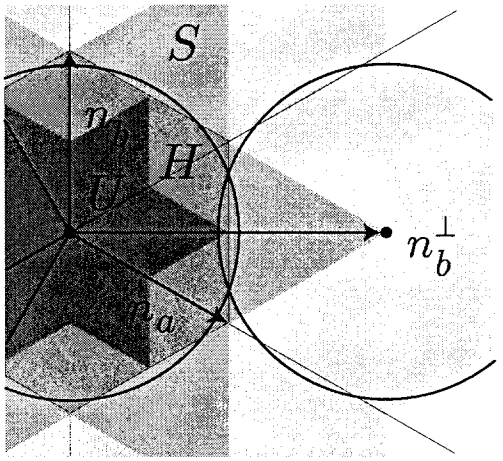

Figure 6.4 Sinusoidal input that lies partly outside H.

in coordinates (4.2).

The reflected sector lies in U for $\theta \in [0, \theta_1]$ and in $H \cap U^c$ for $\theta \in (\theta_1, \theta_2]$. For $\theta \in [0, \theta_1]$, the switching rate is obtained using (6.11) and (6.17) as

$$f_s = \frac{4}{3}\left(1 + r^2 - 2r^2 \cos 2\theta\right) \tag{6.18}$$

For $\theta \in (\theta_1, \theta_2]$, the switching rate is obtained using (6.14) and (6.17) as

$$f_s = 1 + \frac{4}{3} r \left(2r \cos\theta - 1\right)\left(\sqrt{3}\sin\theta - \cos\theta\right) \tag{6.19}$$

Evaluating (6.10) using (6.18) for $\theta \in [0, \theta_1]$, using (6.19) for $\theta \in (\theta_1, \theta_2]$, and using (6.14) for $\theta \in (\theta_2, \pi/6]$ gives

$$\begin{aligned} \hat{f}_s = &-\frac{1}{3} + \frac{2}{\pi}\theta_1 + \frac{8}{\pi}\theta_2 - \frac{16}{\pi} r \left(\cos(\theta_1 - \frac{\pi}{6}) - 2\cos(\theta_2 + \frac{\pi}{6})\right) \\ &- \frac{4}{\pi} r^2 \left(\frac{\pi}{3} - 4\theta_1 - 2\cos(2\theta_1 + \frac{\pi}{6}) + 2\sqrt{3}\cos 2\theta_2\right), \qquad 1/2 < r \leq 1/\sqrt{3}. \end{aligned} \tag{6.20}$$

Formulas (6.12), (6.15), and (6.20) give the average switching rate $\hat{f}_s$ over the range $0 \leq r \leq 1/\sqrt{3}$ and is plotted in Fig. 6.5. For $r = 1/2$ the average switching rate is 0.98732. Fig. 6.5 also plots the minimum and maximum switching rates.

Fig. 6.6 plots the variation of the switching rate against the radius of the sinusoidal input. The switching rate variation for a particular radius is defined as the maximum percentage the switching rate deviates from the average switching rate over the circle normalized to the average switching rate:

$$\text{var}\, f_s(r) = \frac{100}{\hat{f}_s(r)} \max_{0 \leq \theta < 2\pi} |f_s(r, \theta) - \hat{f}_s(r)| \tag{6.21}$$

The maximum variation is 9% at zero radius. Note that the variation never reaches zero. This implies that the contours of Fig. 6.3 are never perfect circles. (Interestingly, the curve rises rapidly beyond $r = 1/2$. This is because in Fig. 6.5 the maximum switching rate is unity for $1/2 \leq r < 1/\sqrt{3}$ while the minimum switching rate decreases fairly rapidly.)

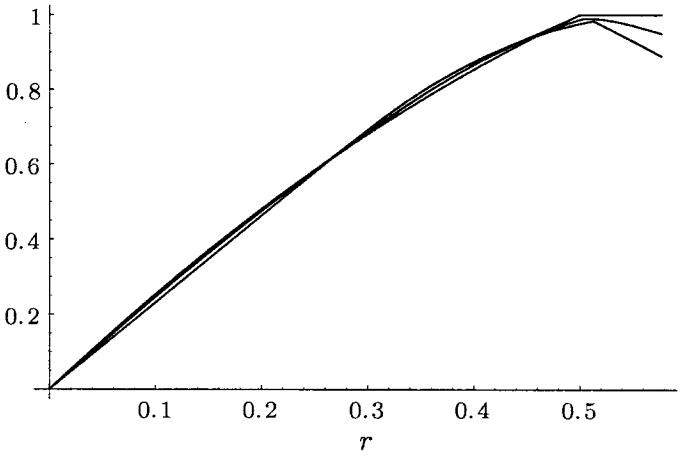

Figure 6.5 Minimum, maximum, and average switching rates for $0 \leq r < 1/\sqrt{3}$.

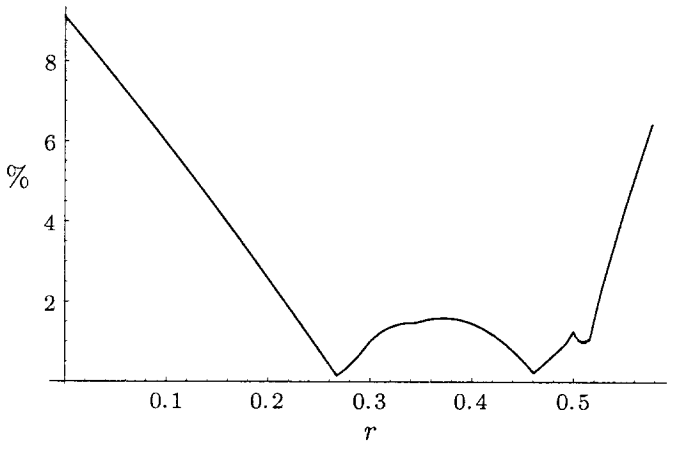

Figure 6.6 Normalized switching rate variation for $0 \leq r < 1/\sqrt{3}$.

Chapter 7

Linear Analysis of $\Sigma\Delta$ Modulators

In this chapter we review the linear analysis of the single-bit single-loop and double-loop $\Sigma\Delta$ modulator as well as the generalization of this analysis to interpolative $\Sigma\Delta$ modulators. In Section 7.4 we extend these results to the vector $\Sigma\Delta$ modulator with hexagonal quantization.

7.1 Single-Loop $\Sigma\Delta$ Modulator

The linear discrete-time model of the scalar $\Sigma\Delta$ modulator (Fig. 2.1) is shown in Fig. 7.1. The integrator is modeled with its discrete-time equivalent and the quantization process is modeled as an additive noise source $e_n = u_n - y_n$. As discussed above, e_n is assumed to be a white, uniform noise source that is statistically uncorrelated with the input.

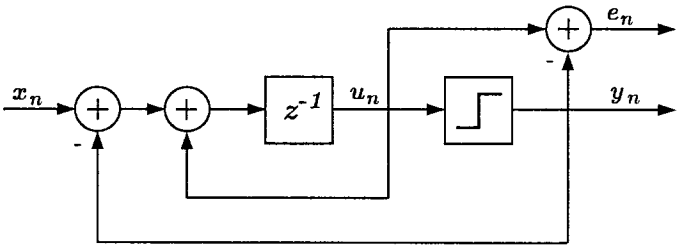

Figure 7.1 Single-Bit, single-Loop $\Sigma\Delta$ modulator.

From Fig. 7.1, one can write the following difference equations that describe the $\Sigma\Delta$ modulator:

$$y_n = z^{-1}x_n + (1 - z^{-1})e_n \tag{7.1}$$

Intuitively, the quantizer output y is the sum of the input signal x (delayed), plus a difference (or discrete time derivative) of the quantization noise e. The principle is that this difference will be a high-frequency term that can be removed by low-pass filtering to obtain the original signal.

If the input signal x is a tone in the baseband, the modulator's output spectrum is similar to that shown in Fig. 7.2 or Fig. 2.6. We see that the low-frequency quantization noise power in the baseband is attenuated relative to its total power. That is, the quantization noise will be pushed or shaped to higher frequencies. This shaping of the noise is advantageous since the high frequency noise can be removed by a low-pass filter.

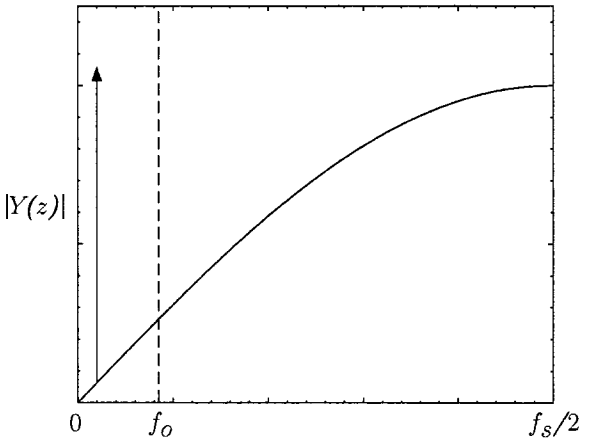

Figure 7.2 Spectral density of the $\Sigma\Delta$ modulator output with an input tone.

7.2 Double-Loop $\Sigma\Delta$ Modulator

Another popular $\Sigma\Delta$ system is the double-loop $\Sigma\Delta$ introduced by Candy [9] and first rigorously analyzed by He [24]. Here, a single-loop $\Sigma\Delta$ is embedded in a second loop with an integrator in the feedforward path as shown in Fig. 7.3. It can be interpreted as a single-loop with the original input replaced by the integrated error between the input and the quantized output. Observe the output of the double-loop $\Sigma\Delta$ modulator is

$$y_n = z^{-1}x_n + (1 - 2z^{-1} + z^{-2})e_n \tag{7.2}$$

In contrast to (7.1) this has the interpretation of being the original signal plus a second-order difference instead of a first-order difference of the single-loop system. A well-known difficulty with the double-loop $\Sigma\Delta$ modulator is the potential for quantizer overload [9].

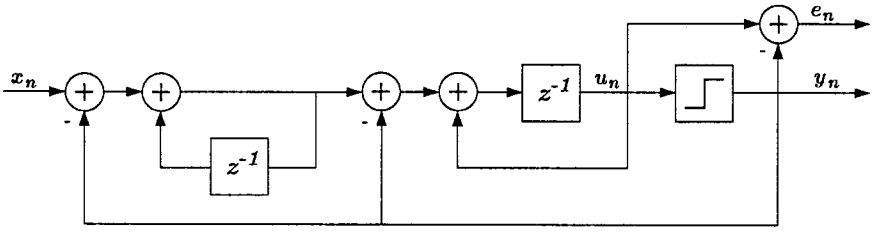

Figure 7.3 Single-Bit Double-Loop $\Sigma\Delta$ modulator.

7.3 Interpolative Modulators

The $\Sigma\Delta$ modulator is one of a variety of specific devices for achieving oversampled analog-to-digital conversion. $\Sigma\Delta$ modulators [1, 3] employ ideal integrators as linear filters. These analog-to-digital converters can be embedded within additional feedback loops to form high-order or multi-loop $\Sigma\Delta$ modulators [9] or cascaded to form multistage $\Sigma\Delta$ modulators [55, 56]. In the single-loop feedback case, a general system can have linear filters in both the feedforward and feedback paths. When the feedback is entirely in the feedback path, the system is called a *predictive coder* [57] of which the delta modulator [58] is a special case. When the filtering is entirely in the feedforward path, the system is called a *noise shaping coder* [57] or *interpolative coder* [29]. The $\Sigma\Delta$ modulator is an interpolative coder with the linear filter specialized to an ideal integrator.

Greater suppression of the quantization noise can be achieved by replacing the integrator with more complex higher-order filters, but the stability of the resulting system must be carefully considered. The resulting architecture is known as an interpolative modulator and is shown in Fig. 7.4. The input feeds a loop filter $G(z)$ that is followed by a binary quantizer. The quantized output y is fed back and subtracted from the input. This forces the average value of the quantized output to follow the average value of the input. Equation (7.1) generalizes to

$$Y(z) = \frac{G(z)}{1+G(z)}X(z) + \frac{1}{1+G(z)}E(z) \tag{7.3}$$

where X, U, E, Y are the z-transforms of x, u, e, y respectively. For example, the choice $G(z) = \frac{1}{z-1}$ yields the modulator of Fig. 7.1. Equation (7.3) is a fundamental relation describing interpolative modulators. It states that the output of the modulator consists of the sum of two terms: the input signal x filtered by the signal transfer function (STF), $\frac{G(z)}{1+G(z)}$ and the quantizer noise e filtered by the noise transfer function (NTF), $\frac{1}{1+G(z)}$. If G is designed properly, the NTF will have a high-pass response, and the STF will be approximately unity in the baseband. In this manner the output SNR in the baseband can be made large [18]. An important consideration in the design of interpolative modulators, especially those of higher order (> 2), is their stability, for large-amplitude low-frequency oscillations can appear [26]. These oscillations can drive the modulator into sustained modes of integrator saturation. Another potential drawback is that higher order filters may require increased hardware complexity [59].

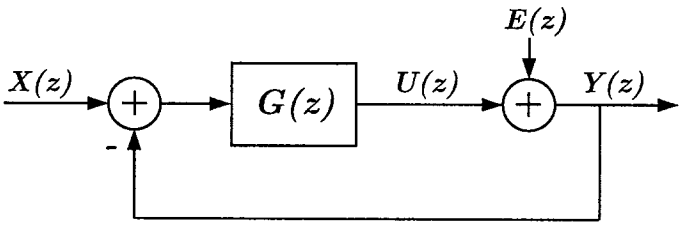

Figure 7.4 Interpolative $\Sigma\Delta$ modulator.

The noise-shaping filter G is usually designed in discrete-time. However, analog modulators have been implemented with op-amps, comparators, and latches. A discrete-time modulator can be converted to an equivalent continuous-time modulator using the impulse-invariant transformation [60, 61, 6].

7.4 Linear Analysis of Vector $\Sigma\Delta$ Modulators with Hexagonal Quantization

A popular measure of modulator performance is the output SNR over the baseband. SNR is mainly governed by the order of the loop filter G and the OSR. The advantage of choosing a higher order filter is an improved SNR for a given OSR. The white noise model can be used to evaluate the spectral density of the modulation noise and the total modulation noise power in the baseband

for the single-loop and double-loop $\Sigma\Delta$ modulators. This calculation is done in [5] for single-bit $\Sigma\Delta$ modulators and is presented in this section for vector $\Sigma\Delta$ modulators.

7.4.1 Linear Model

Define the hexagonal region H of Fig. 7.5 to be the vectors which quantize to zero. H has sides of length $\sqrt{2/3}$ and area $|H| = \sqrt{3}$. Let e_n be a sequence of uncorrelated, zero mean random vectors (i.e. white noise process) that is uniform over the hexagon H and statistically uncorrelated with the input. The power spectral density matrix of e is

$$S_e = \frac{2}{f_s}\frac{1}{|H|}\int_H e\, e^* de = \frac{2}{f_s}\frac{5}{72}P \tag{7.4}$$

where

$$P = \frac{1}{3}\begin{pmatrix} 2 & -1 & -1 \\ -1 & 2 & -1 \\ -1 & -1 & 2 \end{pmatrix}, \tag{7.5}$$

f_s is the sampling rate, and $*$ denotes complex conjugate transpose.

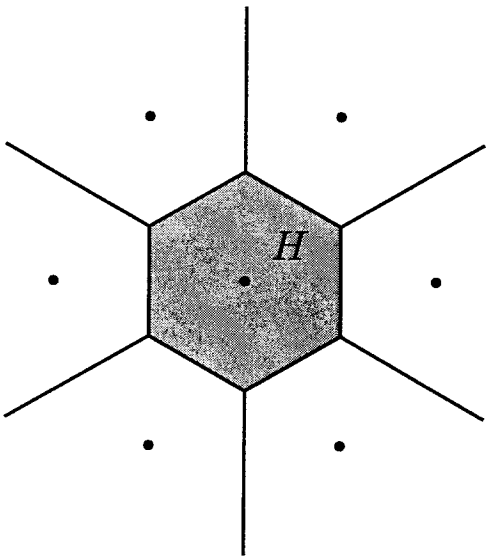

Figure 7.5 Hexagonal vector quantizer, q.

The hexagonal $\Sigma\Delta$ modulator's input/output relation with input vector x_n and output vector y_n is given by

$$y_n = z^{-1}x_n + (1 - z^{-1})e_n \tag{7.6}$$

The output sequence y_n is the sum of the input (delayed) plus a high-frequency term.

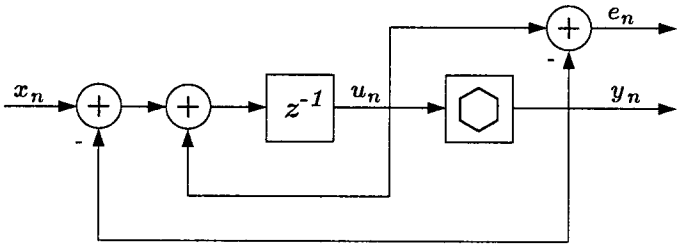

Figure 7.6 Discrete time model of the single-loop hexagonal $\Sigma\Delta$ modulator

As in the single-bit case, we can achieve greater noise suppression by replacing the integrator in Fig. 7.6 with an appropriately designed linear filter as in Fig. 7.4. The operation of this interpolative $\Sigma\Delta$ modulator can be analyzed quantitatively by modeling the quantization process by an additive white noise vector $E(z)$. Then the modulator of Fig. 7.4 is described by the linearized equation

$$Y(z) = (I + G(z))^{-1}G(z)X(z) + (I + G(z))^{-1}E(z) \tag{7.7}$$

where the inverse is a matrix inverse. Similar to the case of a single-bit $\Sigma\Delta$ modulator, equation (7.7) states that the output vector Y consists of two terms: the input signal X filtered by the signal transfer function (STF) matrix $(I + G(z))^{-1}G(z)$ and the quantizer noise E filtered by the noise transfer function (NTF) matrix $(I + G(z))^{-1}$. G can be designed so that the NTF is small in the baseband and the STF is approximately unity in the baseband. In this manner the SNR in the baseband can be made large [18]. Two possible choices of the filter G are:

$$G_1 = \frac{z^{-1}}{1 - z^{-1}}P \tag{7.8}$$

$$G_2 = \frac{z^{-1}(2 - z^{-1})}{1 - 2z^{-1} + z^{-2}}P \tag{7.9}$$

These are vector generalizations of the conventional single-loop modulator, and (up to a prefilter on the input) the conventional double-loop $\Sigma\Delta$ modulator.

This double-loop hexagonal $\Sigma\Delta$ modulator is an adaptation of the modulator proposed by Candy in [9] and is superior to the single-loop hexagonal $\Sigma\Delta$ modulator because it only requires a moderate increase in circuit complexity, and yet it achieves a 15 dB/octave tradeoff between SNR and OSR, whereas the single-loop hexagonal $\Sigma\Delta$ modulator achieves only 9 dB/octave. Furthermore, both modulators have the same stable input range (dynamic range).

A typical simulated output line-neutral waveform (reference superimposed) and spectrum for the double-loop hexagonal $\Sigma\Delta$ modulator is shown in Fig. 7.7 and Fig. 7.8 respectively. The OSR is 64 and the input amplitude is 80% of the full-scale linear range. Note that in contrast to the single-loop case, the double-loop hexagonal $\Sigma\Delta$ modulator produces more non-adjacent transitions.

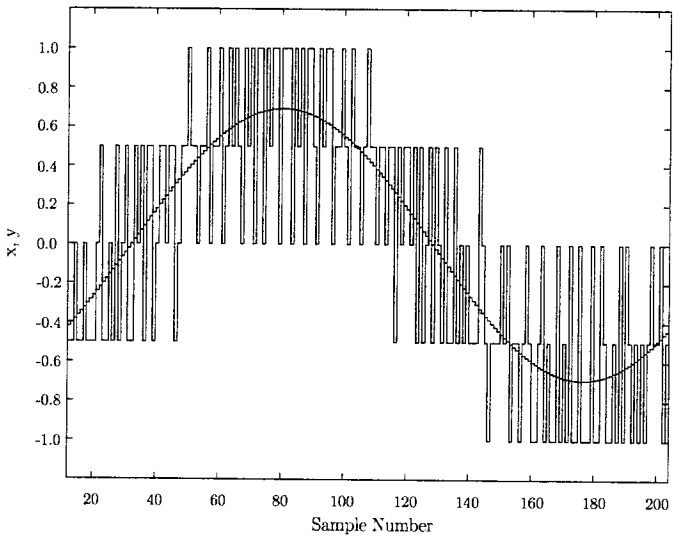

Figure 7.7 Waveform of a double-loop hexagonal VSI $\Sigma\Delta$ modulator.

7.4.2 Modulation Noise Analysis

Recall that if L is a multivariate linear filter with transfer function matrix $B(f)$ and $y(t) = L(x(t))$, then the spectral density matrix functions of the input and output are related by the expression [62]

$$S_y(f) = B(f)S_x(f)B(f)^* \tag{7.10}$$

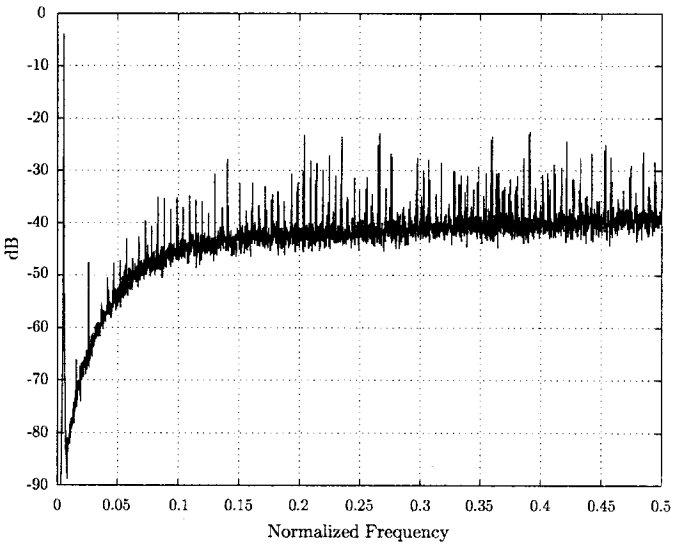

Figure 7.8 Spectrum of a double-loop hexagonal VSI $\Sigma\Delta$ modulator.

The modulation noise vector, n is the quantization error vector, e filtered by the NTF matrix. For the single-loop hexagonal $\Sigma\Delta$ modulator, the spectral density of the modulation noise is

$$\begin{aligned} S_n(f) &= \left(I + G_1(e^{i2\pi f/f_s})\right)^{-1} S_e \left(I + G_1^*(e^{i2\pi f/f_s})\right)^{-1} \\ &= 4\sin^2(\pi f/f_s)\, S_e \end{aligned} \tag{7.11}$$

Then the modulation noise power for the single-loop hexagonal $\Sigma\Delta$ modulator in the baseband $0 \leq f < f_0$ is

$$\sigma_n^2 = \int_0^{f_0} S_n(f)df \approx \frac{5\pi^2}{72}\mathrm{OSR}^{-3}P, \quad f_s^2 \gg f_0^2 \tag{7.12}$$

Similarly, for the double-loop hexagonal $\Sigma\Delta$ modulator, the modulation baseband noise power can be shown to be

$$\sigma_n^2 \approx \frac{\pi^4}{24}\mathrm{OSR}^{-5}P, \quad f_s^4 \gg f_0^4 \tag{7.13}$$

Fig. 7.9 shows SNR curves for the single-loop and double-loop $\Sigma\Delta$ modulator versus OSR. A sine wave input of full-scale linear range amplitude is used. These graphs are derived from (7.12) and (7.13) and demonstrate that as modulator order increases the lines become steeper; this implies that the double-loop filter realizes higher resolution from oversampling.

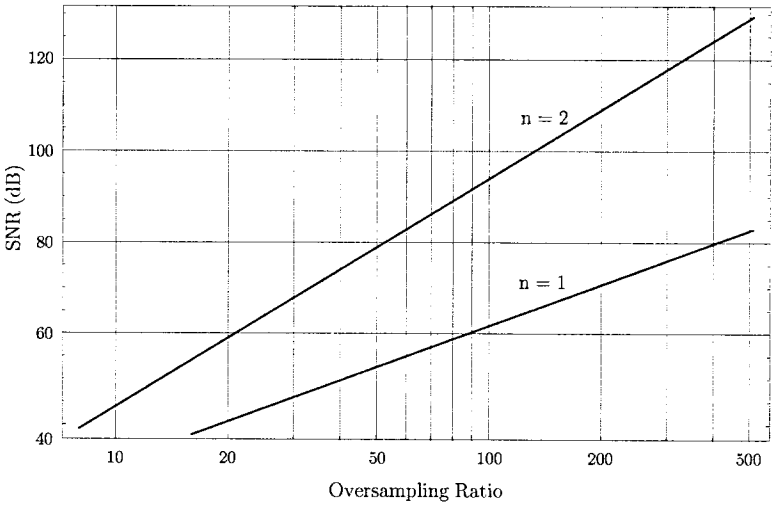

Figure 7.9 SNR as a function of OSR for single-loop and double-loop hexagonal $\Sigma\Delta$ modulators.

7.4.3 Dynamic Range

The trackable input signal range for the single-loop and double-loop hexagonal $\Sigma\Delta$ modulators is the shaded hexagon which passes through the outer six output space vectors of Fig. 7.10. When the input signal exceeds this range, the modulator's integrators wind-up. However, overmodulation causes the input signal to exceed the stable range. To address this problem, limiters may be placed on the input signal to ensure it remains in the shaded region. This stabilization technique ensures that the output voltage waveforms gradually degrade into six-step mode as the input signal is increased beyond the stable input signal range. This technique may also be applied to higher-order (> 2) modulators which always have the potential for oscillation when the input exceeds the stable input range [18, 28].

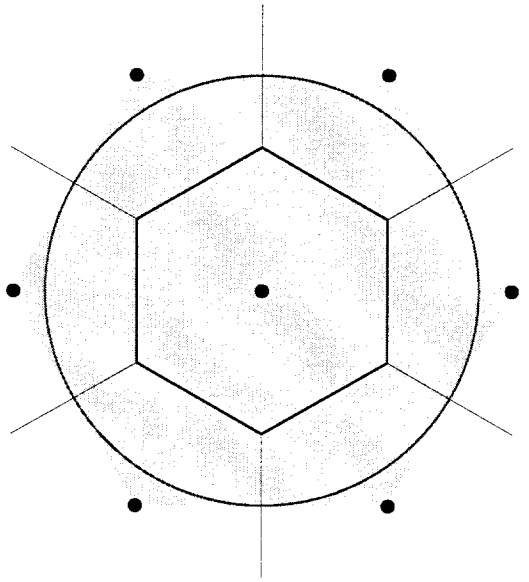

Figure 7.10 Stable input signal range and boundary of the linear range for the hexagonal $\Sigma\Delta$ modulator.

A parameter of interest in power electronics is the range within which the $\Sigma\Delta$ modulator is linear for sinusoidal inputs. For the hexagonal $\Sigma\Delta$ modulator, the boundary of the linear range is given by the inscribed circle of the shaded hexagon in Fig. 7.10. This boundary coincides with the linear range of space vector PWM, which is $2/\sqrt{3}$ larger than the linear range of sine-triangle PWM and the threefold-scalar $\Sigma\Delta$ modulator [10, 46, 63].

Chapter 8

Simulation And Hardware Results

This chapter first presents simulation results computed with MATHEMATICA that numerically confirm the analytic formulae for the quantization error and output spectra, and average switching rate of the hexagonal $\Sigma\Delta$ modulator. We then discuss aspects of a MATLAB based toolbox for computation of the SNR versus input amplitude, and average switch rate. Thirdly, this chapter provides hardware results pertaining to the application of various $\Sigma\Delta$ modulators to the resonant dc link converter. Finally, we briefly detail two hardware implementations of $\Sigma\Delta$ modulators for power electronic applications.

8.1 Quantization Error

Numerical results for 1024 samples of the quantization error sequence e_n are obtained using recursion (4.13). Fig. 8.1 shows the a-component of e_n for $\beta = (0.229693, 0.339432, -0.569125)$ and $e_0 = 0$. The components of β are allowed a precision of 30 digits so that they resemble irrational numbers.

The discrete Fourier transform of the error sequence is taken with a normalized frequency such that the sampling frequency equals one. The spectral density is evaluated at 1024 frequencies uniformly distributed in the range $[0, 1)$ and is denoted by triangles in Fig. 8.2. Fig. 8.2 also shows the Bohr-Fourier spectrum predicted by formula (4.34) as boxes. The theoretical and simulated points correspond quite closely. Note that the discrete Fourier transform of the numerical results is computed at uniformly spaced frequencies whereas the Bohr-Fourier spectrum is computed for the frequencies $\langle p\beta \rangle$ with $p \in \Lambda^*$. The locations of the spikes correspond well, but their amplitudes

differ somewhat. As expected, the error spectrum is neither continuous nor white. The quantization error sequence has mean 6.64×10^{-4} and variance 9.27×10^{-2} which agrees well with the theoretical results of section 4.9. The quantization error sequence mean and variance are close to that of a uniform sequence of random variables.

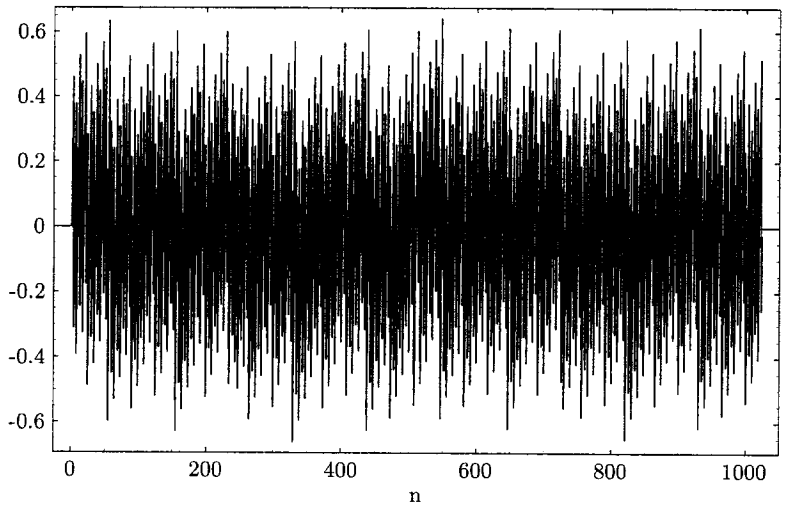

Figure 8.1 Simulated quantization error sequence e_n.

8.2 Quantizer Output

We present simulation results of the power spectral density of the quantizer output of the hexagonal $\Sigma\Delta$ modulator. The simulation parameters are identical to section 8.1. The simulated spectral density of the first component (i.e. a-component) of the quantization output sequence,

$$q_{n+1} = e_n - e_{n+1} + \beta \tag{8.1}$$

for constant input is shown in Fig. 8.3.

The discrete Fourier transform of the output sequence is taken with a normalized frequency such that the sampling frequency equals one. The power spectral density is evaluated at 1024 frequencies uniformly distributed in the range $[0, 1)$ and is denoted by triangles in Fig. 8.4.

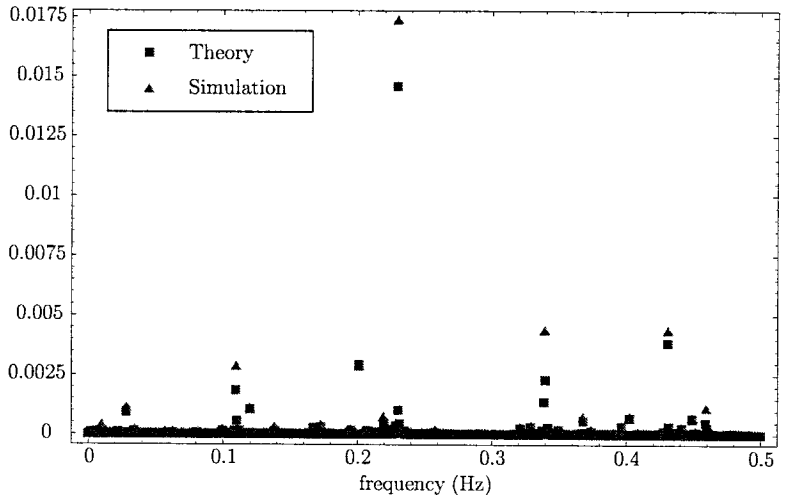

Figure 8.2 Simulated and theoretical spectrum S_e of quantization error.

The spectral coefficients predicted by (4.35) are denoted as boxes in Fig. 8.4. As with the quantization error, the theoretical and simulated points correspond quite closely, even though the number of sample points is only 1024.

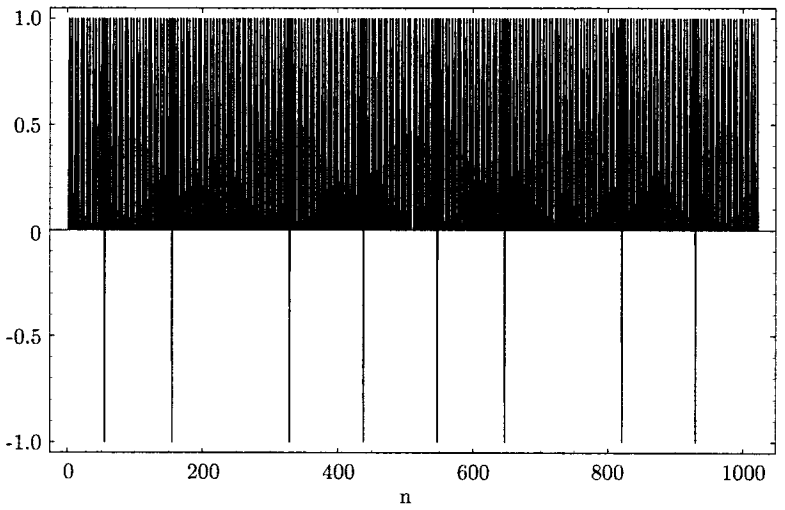

Figure 8.3 Simulated output sequence.

8.3 Average Switch Rate

Fig. 8.5 shows the simulated average switching rate for sinusoidal inputs of amplitudes $0 \leq r < 1/\sqrt{3}$ compared to the average switching rate $\hat{f}_s$ computed from formulas (6.12), (6.15), and (6.20). The simulation length is 65,536 points and the oversampling ratio is 64. The absolute maximum error between simulation and $\hat{f}_s$ is 4.24×10^{-2} at $r = 0.128$ and the mean-squared error is 1.88×10^{-4}. The error can be reduced by increasing the oversampling ratio. For instance the mean-squared error reduces to 6.85×10^{-5} for an oversampling ratio of 256.

8.4 Simulation of the Hexagonal $\Sigma\Delta$ Modulator

The following results were obtained from an adaptation of Richard Schreier's MATLAB Delta-Sigma toolbox [64]. The SNR versus input amplitude plot for a double-loop hexagonal $\Sigma\Delta$ modulator with an OSR of 32 is shown in Fig. 8.6. The procedure to generate this graph is: First, simulate

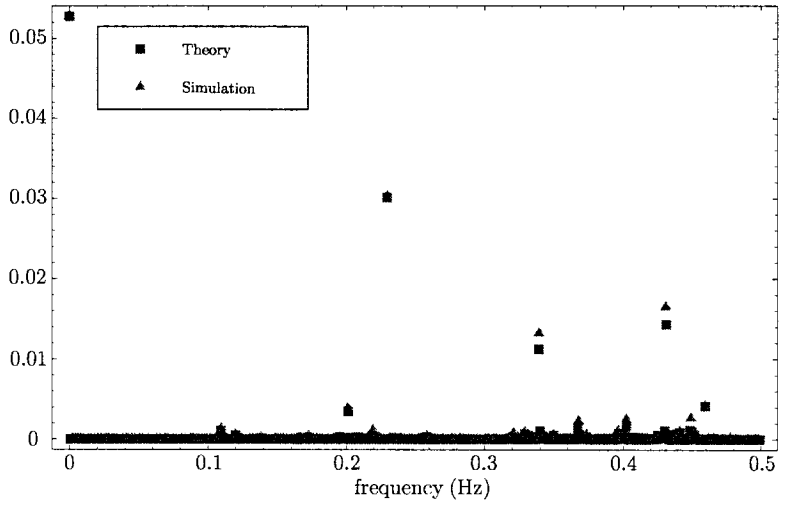

Figure 8.4 Power spectrum of simulated output sequence and the theoretically predicted spectral coefficients.

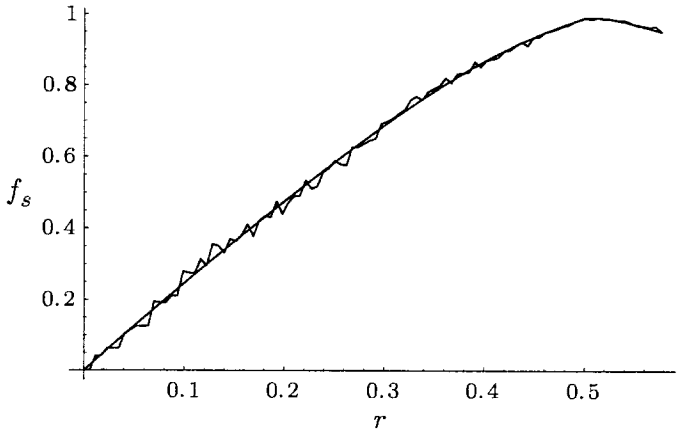

Figure 8.5 Average switching rate simulation results and $\hat{f}_s$ for $0 \leq r < 1/\sqrt{3}$.

modulator output sequences of length 8192 for a set of input tones. Second, Hann-windowed FFTs are computed for each input tone. Finally, the SNR is calculated as the the ratio of the sine wave power to the power in all in-band bins other than those associated with the input tone.

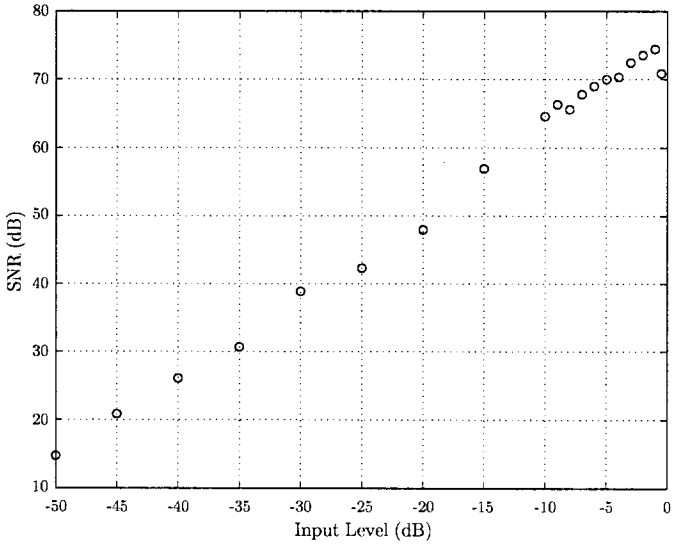

Figure 8.6 SNR versus input level for double-loop hexagonal ΣΔ modulator with OSR=32.

Switching rate is an important performance measure in power electronic design since device switching loss is directly proportional to switching rate. Fig. 8.7 shows the simulated average switching rate for sinusoidal inputs of amplitudes within the linear range. The simulation length is 65,536 points and the OSR is 64. In Fig. 8.7 the lower curve and upper curve are the single-loop and double-loop hexagonal ΣΔ modulators.

8.5 Resonant Link Converters

In power electronics, ΣΔ modulators have been applied successfully to systems such as resonant link converters (Fig. 8.8) where the discrete timing of the circuit switching precludes the use of conventional modulation techniques such as pulse-width modulation (PWM). Resonant link converters use zero voltage switching to limit switching losses and allow much higher switching frequencies.

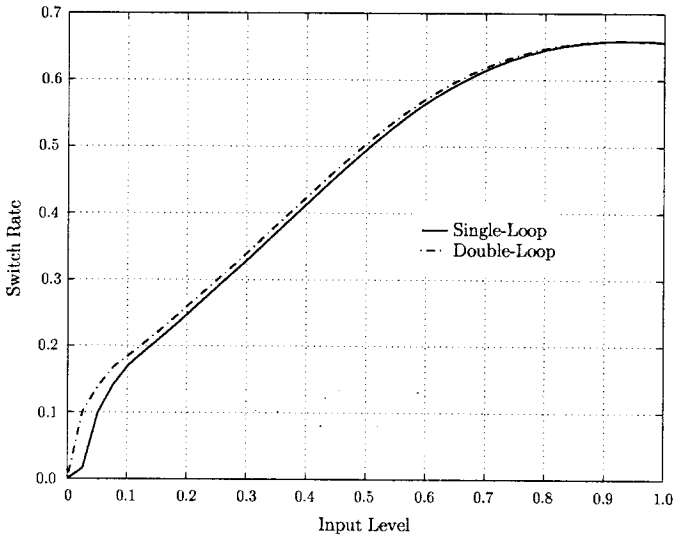

Figure 8.7 Switching rate versus input level for the single-loop and double-loop hexagonal $\Sigma\Delta$ modulator with an OSR of 64.

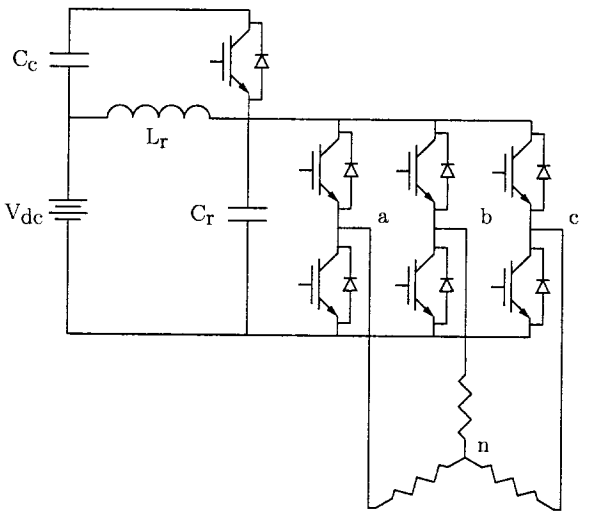

Figure 8.8 Resonant dc link inverter schematic.

An interpolative modulator suitable to the RDCL is shown in Fig. 8.9. This modulator is the same as the VSI modulator of Fig. 2.4 with the exceptions that a linear filter G replaces the analog integrator, and the latch is clocked at the zero-voltage instants of the RDCL bus instead of a constant rate f_s. Inherent to the RDCL is the resonant pulse width irregularity and resultant irregularity (jitter) of zero-voltage instants [12].

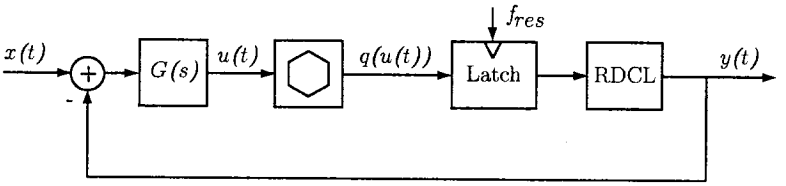

Figure 8.9 Resonant dc link interpolative modulator.

One motivation for $\Sigma\Delta$ modulation of the resonant dc link inverter (Fig. 8.8) is the spectral performance that can be achieved. Experimental and simulation results for a 40 kVA, 75 kHz actively clamped resonant dc link inverter using single and double-loop $\Sigma\Delta$ modulators with a resonant frequency of 75 kHz and a control bandwidth (base band) of 2 kHz are given in our paper [10].

More recent results for RDCL inverter employing single-loop and double-loop hexagonal $\Sigma\Delta$ modulation and a bandpass interpolative modulator are given below. The resonant pulse frequency is 75 kHz and the output drives a light passive inductive-resistive load ($< 10\%$ rated current). This modulation system was implemented in a digital signal processor (DSP) and field programmable gate array (FPGA). A half-scale, three-phase balanced sinusoidal input with and frequency 60 Hz is used throughout.

The output line-neutral voltage waveforms and spectra for single-loop, double-loop, and band-pass hexagonal $\Sigma\Delta$ modulators are shown in Fig. 8.10 and Fig. 8.11; Fig. 8.12 and Fig. 8.13; and Fig. 8.14 and Fig. 8.15, respectively. Note the broadband spectrum which contrasts with the discrete spectrum of PWM.

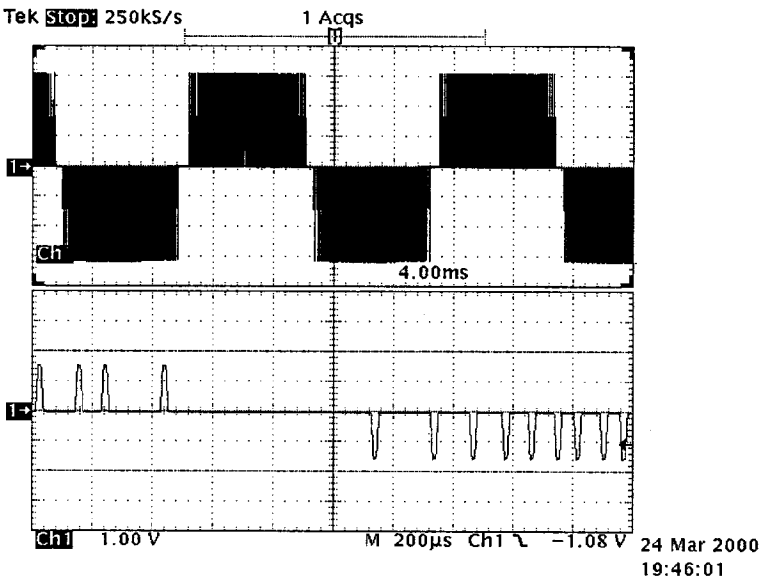

Figure 8.10 RDCL with single-loop hexagonal ΣΔ modulator waveform.

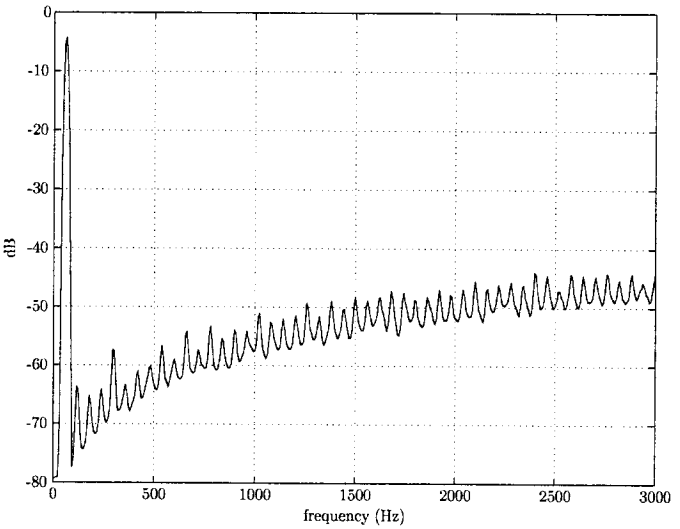

Figure 8.11 RDCL with single-loop hexagonal ΣΔ modulator spectrum.

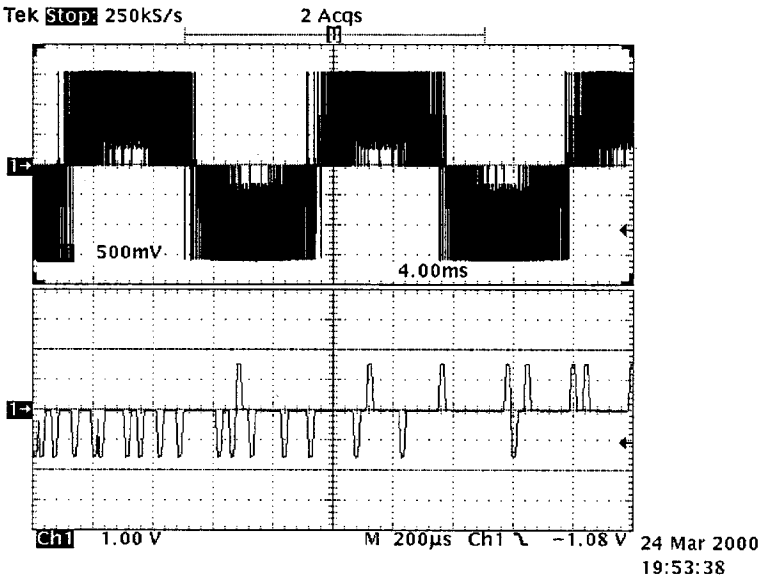

Figure 8.12 RDCL with double-loop hexagonal ΣΔ modulator waveform.

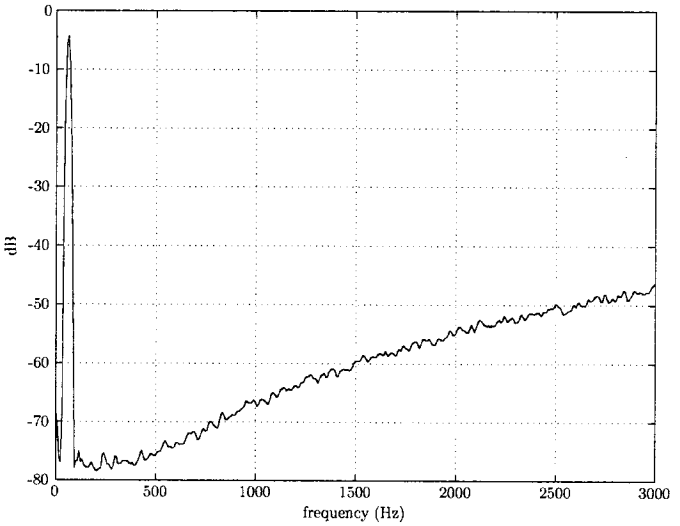

Figure 8.13 RDCL with double-loop hexagonal ΣΔ modulator spectrum.

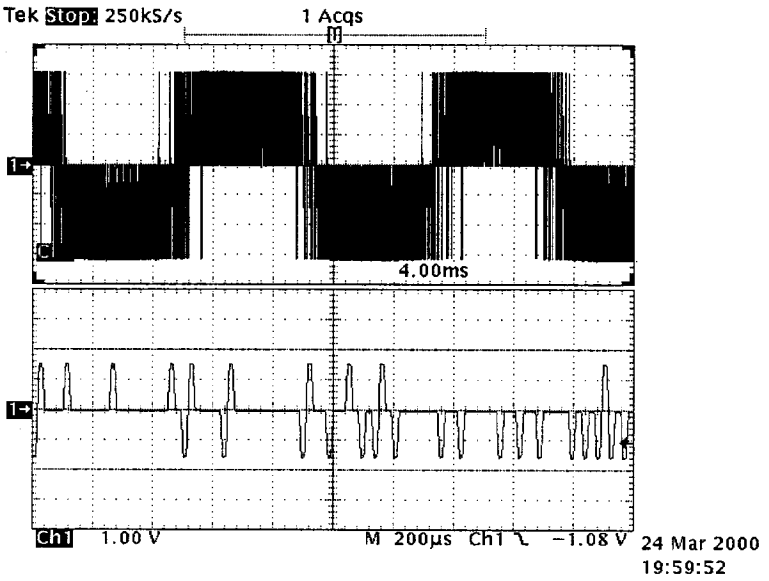

Figure 8.14 RDCL with band-pass hexagonal ΣΔ modulator waveform.

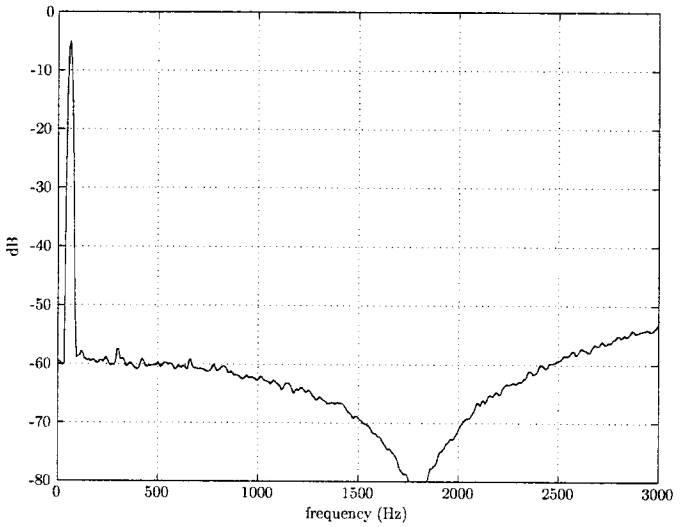

Figure 8.15 RDCL with band-pass hexagonal ΣΔ modulator spectrum.

8.6 ΣΔ Modulator Implementations

The hardware implementation of the hexagonal ΣΔ modulator has gone through two generations. The first generation modulator was implemented in analog form as shown in Fig. 8.16. A reference is generated by the DSP and sent to the analog ΣΔ modulator through a D/A converter. The modulator loop consists of a filter implemented with three op-amps, hexagonal quantizer implemented with nine comparators, three latches, and an analog multiplexor to synthesize the modulator feedback from the switch states and resonant voltage V_{Cr}. Finally, the modulator output, which represents the switch states, is sent to the semiconductor devices via gate drive circuitry. The modulator is clocked and the semiconductor devices are switched at the zero instants of the resonant voltage to minimize the semiconductor switching losses. In hard-switched VSI applications the modulator is clocked at a fixed rate.

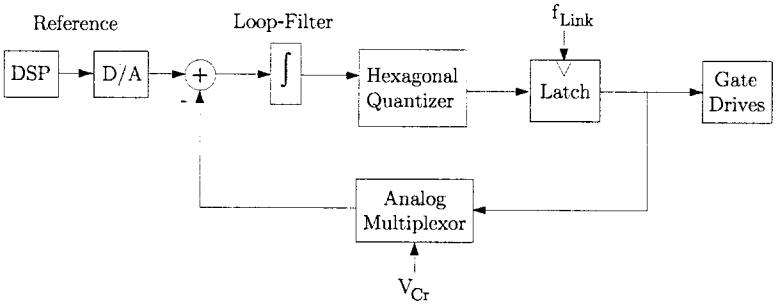

Figure 8.16 Analog Hexagonal ΣΔ Modulator.

The second-generation modulator was implemented in digital form as shown in Fig. 8.17. A 60MHz TMS320C32 DSP implements the modulator. The ΣΔ modulator lends itself well to software implementation because of its algorithmic nature [46, 63]. Also, note that unlike PWM, a ΣΔ modulator does not require high-resolution hardware timers other than a low-resolution timer to set the sampling rate of the modulator routine. The loop filter, quantizer, and reference are generated by and are internal to the DSP. The quantizer feedback is synthesized in the DSP by sampling the integral of the resonant bus voltage, V_{Cr} at the link frequency. The output switch states of the modulator is generated internal to the DSP and is written directly to the field programmable gate

array (FPGA) where the switch states are latched at the link frequency and then sent to the gate drive circuitry.

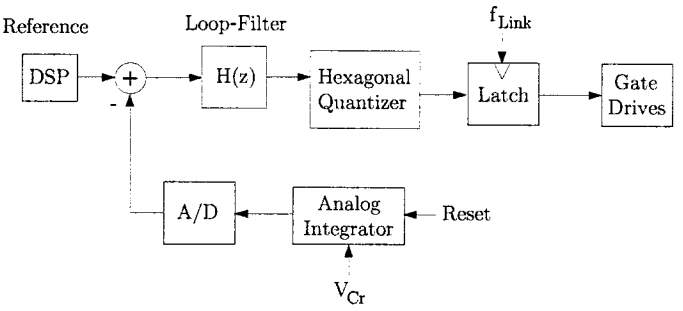

Figure 8.17 Digital Hexagonal ΣΔ Modulator.

Chapter 9

Conclusions and Future Work

In general there is a history of methods devised in communications such as PWM being effective when adapted and applied to power electronics. In this dissertation, we think of the power electronic circuit acting as an analog-to-digital converter. Switching states in power electronic circuits may be thought of as determining quantized outputs which are passed through a low pass filter to synthesize a given input signal. This process is analogous to quantizing, transmitting and demodulating signals in communication systems. Pursuit of this analogy in the context of $\Sigma\Delta$ modulation with a natural choice of a nearest neighbor quantizer yields a hexagonal $\Sigma\Delta$ modulator for a voltage source inverter that is a nontrivial generalization of a scalar $\Sigma\Delta$ modulator. In particular, we formulate the problem of reproducing a desired signal with a high frequency power electronic circuit by regarding the circuit as performing quantization in an interpolative $\Sigma\Delta$ modulator. The binary quantizers of conventional scalar $\Sigma\Delta$ modulators generalize easily to the vector quantizers appropriate to power electronic circuit topologies.

The output spectrum and switching rate of the hexagonal $\Sigma\Delta$ modulator have complicated behavior and are key performance measures. We have applied ergodic theory and Fourier analysis to analytically compute the output spectrum and switching rate. We have found the interplay between the hexagonal geometry and the intricacies of the ergodic and harmonic analysis to be intriguing. These calculations are foundational for hexagonal $\Sigma\Delta$ modulators and for their application to power electronics.

Viewing high frequency power electronic circuits as performing quantization allows them to be regarded as part of the modulator topology (Fig. 2.4). Then noise-shaping methods from communications theory can then be applied to shape the quantization noise so that it is pushed to higher frequencies and will be attenuated by the load.

$\Sigma\Delta$ modulation is well established in communications and higher order $\Sigma\Delta$ modulator architectures [28, 29, 65] and stability issues [26, 18] are discussed extensively in the communications literature. We have found that these more complex architectures can similarly be extended to the vector case and in particular to modulators with hexagonal quantization. Thus we propose single-loop and double-loop hexagonal $\Sigma\Delta$ vector modulator designs for a VSI. Analysis and simulation of these designs show that the approach yields significant improvements in spectral performance.

A new $\Sigma\Delta$ modulator for power electronic applications was invented by generalizing the ideas from scalar $\Sigma\Delta$ modulators that are applied in communications and signal processing. The power electronic circuitry requires the conventional binary quantizer to be generalized to a hexagonal quantizer of vector signals. Specifically, this work makes the following contributions:

- The insight that a power electronic circuit may be thought of as an analog-to-digital converter in which the analog input is the signal to be synthesized and the quantized digital output is the state of the circuit switches.

- Invention of the hexagonal $\Sigma\Delta$ modulator as well as the extension to double-loop and interpolative $\Sigma\Delta$ architectures. This work represents a significant improvement in spectral performance over prior work in power electronics.

- Rigorous derivations of the hexagonal $\Sigma\Delta$ modulator's output and error spectra, autocorrelation, mean, and variance for generic and non-generic constant inputs using ergodic theory and Fourier series on the hexagon. These results are corroborated numerically.

- Generalization of the conventional white noise analysis of a scalar $\Sigma\Delta$ modulator to the hexagonal $\Sigma\Delta$ modulator.

- Derivation of the switching frequency of scalar $\Sigma\Delta$ modulator and generalization to the hexagonal case. This result is of practical interest in power applications since switching frequency is directly related to semiconductor power loss.
- Adaptation of Richard Schreier's MATLAB Delta-Sigma toolbox [64] for the hexagonal $\Sigma\Delta$ modulator. This is a useful design and analysis tool.
- Development of a set of MATHEMATICA programs for lattice generation; and computation of the hexagonal Fourier series, switching rate, autocorrelation, and spectra.
- Demonstration of hardware and simulation results which significantly improve the spectral characteristics of power electronic converters. Single and double-loop hexagonal $\Sigma\Delta$ modulators as well as variations thereof in analog and digital forms have been implemented in hardware. These modulators are currently manufactured at Soft Switching Technologies, Madison, WI for spectrally demanding commercial power electronic applications.
- Adaptation of $\Sigma\Delta$ modulation technology to a host of applications including electric submarines and vehicles, solar distribution systems, active filters, aircraft frequency converters, and wind turbines.

The publications produced are a patent [47], a submitted journal article [48], a journal article in preparation [32], and two conference papers [10, 27].

9.1 Open Problems and Suggestions for Future Work

Future work includes:

1. Attempt various generalizations of the spectral analysis of Chap. 4. For example, the analysis could consider sinusoidal inputs, or second order modulators, or the effect of the "diameter" of the central hexagon region. (Sinusoidal inputs are a practical case, showing that quantization error of the double-loop modulator is white would validate the use of the white-noise approximation, and experimental results suggest that the "diameter" of the central hexagon region has a significant impact on the output spectrum.)

2. Explore other potential applications in power electronics and elsewhere. In power electronics, the hysteretic modulator appears to have much in common with the $\Sigma\Delta$ modulators, but has not been rigorously analyzed. Perhaps the methods similar to those employed in Chap. 4 would apply to the hysteretic modulator to derive its spectrum. This modulator is shown in Fig. 9.1 and is identical to $\Sigma\Delta$ with the exception that the comparator and single-bit latch are replaced by a single-bit hysteretic comparator. Thus, the system is no longer synchronously sampled. Instead the output flips according to the integrator state. Outside power electronics, explore the application of vector $\Sigma\Delta$ modulation to fields such as color imaging [66], sonar, and acoustics.

3. Within the context of control systems, apply the linear model of the $\Sigma\Delta$ modulator to investigate the stability and spectra of the overall system. Consider the dc/ac power conversion system shown in Fig. 9.2. The system consists of a full-bridge resonant dc link converter driving a second-order low-pass output filter and passive first-order load. The control objective is for the filter capacitor voltage V_{C_f} to track a 0–73 Hz sinusoidal reference with a maximum SNR of 60 dB over the baseband of 820 Hz. More generally, this system is an instance of the control block diagram of Fig. 9.3 wherein the design consists of choosing a suitable modulator, state feedback k, and compensator G to meet the control objectives.

4. Inherent to the RDCL is the resonant pulse width irregularity and resultant irregularity (jitter) of zero-voltage instants [12]. Attempts to quantify the effects of jitter for the $\Sigma\Delta$ modulator have been reported [67].

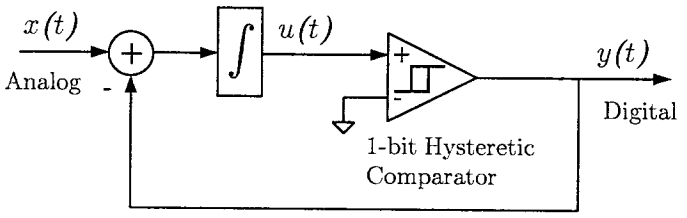

Figure 9.1 Hysteretic modulator.

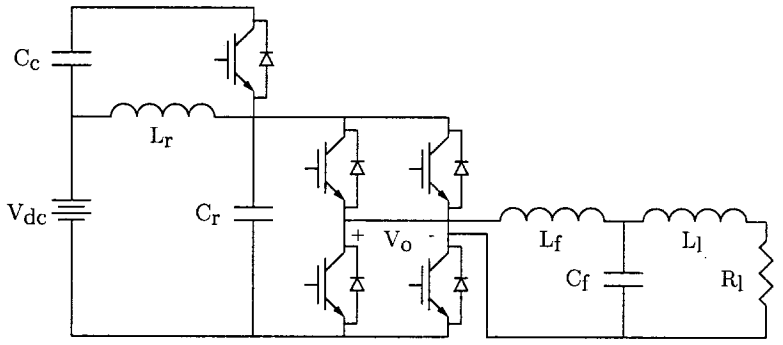

Figure 9.2 A dc/ac power conversion system.

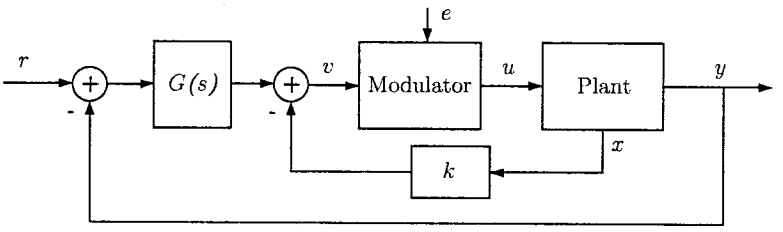

Figure 9.3 System block diagram.

LIST OF REFERENCES

[1] C.C. Cutler, "Transmission systems employing quantization," 1960 U.S. Patent No. 2927962.

[2] H. Inose, Y. Yasuda, and J. Murakami, "A telemetering system by code modulation–$\Sigma\Delta$ modulation," *IRE Trans. Space Elec. Tele.*, pp. 204–209, Sept. 1962.

[3] H. Inose and Y. Yasuda, "A unity bit coding method by negative feedback," *Proc. IEEE*, vol. 51, pp. 1524–1535, Nov. 1963.

[4] H.A. Spang and P.M. Schultheiss, "Reduction of quantizing noise by use of feedback," *IRE Trans. Comm. Syst.*, pp. 373–380, Dec. 1962.

[5] J.C. Candy and G.C. Temes (Eds.), *Oversampling Methods for A/D and D/A Conversion*, IEEE Press, NJ, 1992.

[6] S.R. Norsworthy, R. Schreier, and G.C. Temes (Eds.), *Delta-Sigma Data Converters: Theory, Design, and Simulation*, IEEE Press, NJ, 1997.

[7] J.C. Candy, "A use of limit cycle oscillation to obtain robust analog-to-digital converters," *IEEE Trans. Commun.*, vol. COM-22, pp. 298–305, Mar. 1974.

[8] J.C. Candy and O.J. Benjamin, "The structure of quantization noise from sigma-delta modulation," *IEEE Trans. Commun.*, vol. COM-29, pp. 1316–1323, Sept. 1981.

[9] J.C. Candy, "A use of double integration in sigma delta modulation," *IEEE Trans. Commun.*, vol. COM-33, no. 3, pp. 249–258, Mar. 1985.

[10] G. Luckjiff, I. Dobson, and D. Divan, "Interpolative sigma-delta modulators for high frequency power electronic applications," in *Proc. Power Electronics Specialists Conf.*, Atlanta, June 1995, pp. 444–449.

[11] T.G. Habetler and D.M. Divan, "Performance characterization of a new discrete pulse modulated current regulator," in *Proc. Ind. Appl. Soc.*, Pittsburgh, Oct. 1988, pp. 395–405.

[12] D.M. Divan, "The resonant dc link converter," in *Proc. Ind. Appl. Soc.*, Denver, 1986, pp. 648–656.

[13] H. Van Der Broeck, H. Skudelny, and G. Stanke, "Analysis and realization of a pulsewidth modulator based on voltage space vectors," *IEEE Trans. Ind. Appl.*, vol. 24, no. 1, pp. 142–150, Feb. 1988.

[14] J.H. Conway and N.J.A. Sloane, *Sphere Packings, Lattices and Groups*, Springer-Verlag, NY, second edition, 1993.

[15] A. Gersho, "On the structure of vector quantizers," *IEEE Trans. Inform. Theory*, vol. IT-28, pp. 157–166, Mar. 1982.

[16] A. Gersho and R.M. Gray, *Vector Quantization and Signal Compression*, Kluwer Academic, Boston, 1992.

[17] W.R. Bennett, "Spectra of quantized signals," *Bell Syst. Tech. J.*, vol. 27, pp. 446–472, July 1948.

[18] R. Schreier, "An empirical study of high order single bit delta sigma modulators," *IEEE Trans. Circuits Syst.*, vol. 40, no. 8, pp. 461–466, Aug. 1993.

[19] R.M. Gray, "Spectral analysis of quantization noise in a single-loop sigma-delta modulator with dc input," *IEEE Trans. Commun.*, vol. 37, no. 6, pp. 588–599, June 1989.

[20] R.M. Gray, "Oversampled sigma-delta modulation," *IEEE Trans. Commun.*, vol. COM-35, no. 5, pp. 481–488, July 1987.

[21] R.M. Gray, "Quantization noise spectra," *IEEE Trans. Inform. Theory*, vol. 36, no. 6, pp. 1220–1244, Nov. 1990.

[22] D.F. Delchamps, "Exact asymptotic statistics for sigma-delta quantization noise," in *Proc. Allerton Conf. Commun., Contr., and Computing*, Urbana, Oct. 1990, pp. 703–712.

[23] D.F. Delchamps, "Spectral analysis of sigma-delta quantization noise," in *Proc. Inform. Sciences and Syst.*, Johns Hopkins University, Baltimore, Mar. 1990.

[24] N. He, F. Kuhlmann, and A. Buzo, "Double-loop sigma-delta modulation with dc input," *IEEE Trans. Commun.*, vol. COM-38, pp. 106–114, Apr. 1990.

[25] J.C. Kieffer, "Analysis of dc input response for a class of one-bit feedback encoders," *IEEE Trans. Commun.*, vol. COM-38, no. 3, pp. 337–340, Mar. 1990.

[26] S. Hein and A. Zakhor, "On the stability of sigma-delta modulators," *IEEE Trans. Signal Processing*, vol. 41, no. 7, pp. 2322–2348, July 1993.

[27] G. Luckjiff and I. Dobson, "Power spectrum of a sigma-delta modulator with hexagonal vector quantization and dc input," in *Proc. Int. Symp. on Circuits and Systems*, Orlando, May 1999.

[28] R.W. Adams, P.F. Ferguson, A. Ganesan, S. Vincelette, A. Volpe, and R. Libert, "Theory and practical implementation of a fifth order sigma delta A/D converter," *J. Audio Eng. Soc.*, vol. 39, no. 7, pp. 515–528, July 1991.

[29] K.C.-H Chao, S. Nadeem, W.L. Lee, and C.G. Sodini, "A higher order topology for interpolative modulators for oversampling A/D converters," *IEEE Trans. Commun.*, vol. 37, no. 3, pp. 309–318, Mar. 1990.

[30] N. He, F. Kuhlmann, and A. Buzo, "Multiloop sigma-delta quantization," *IEEE Trans. Inform. Theory*, vol. 38, no. 3, pp. 1015–1028, May 1992.

[31] I. Galton, "Granular quantization noise in a class of delta-sigma modulators," *IEEE Trans. Inform. Theory*, vol. 40, no. 3, pp. 848–859, May 1994.

[32] G. Luckjiff and I. Dobson, "Sigma-delta modulators for power electronic applications," *In preparation for IEEE Trans. Power Electronics*, 2003.

[33] A. Boehringer and F. Brugger, "Transformatorlose transistor-pulsumrichter mit ausgangsleistungen bis 50 kva," *E&M*, vol. 96, no. 12, pp. 538–545, 1979.

[34] B. Schwarz, *Beiträge zu reaktionsschnellen und hochgenauen drehstrom-positioniersystemen*, Dissertation, Universität Stuttgart, 1986.

[35] M. Kheraluwala and D.M. Divan, "Delta modulation strategies for resonant link inverters," in *Proc. Power Electronics Specialists Conf.*, June 1987, pp. 271–278.

[36] D.R. Seidl, *Motion and Motor Control Using Structured Neural Networks*, Ph.D. dissertation, University of Wisconsin-Madison, 1996.

[37] G. Venkataramanan, D.M. Divan, and T.M. Jahns, "Discrete pulse modulation strategies for high-frequency inverter systems," in *Proc. Power Electronics Specialists Conf.*, June 1989, pp. 1013–1020.

[38] V.I. Utkin, *Sliding Modes and their Applications in Variable Structure Systems*, MIr Publishers, Moscow, 1978.

[39] G. Venkataramanan and D.M. Divan, "Discrete time integral sliding mode control for discrete pulse modulated converters," in *Proc. Power Electronics Specialists Conf.*, June 1990, pp. 67–73.

[40] A. Mertens, "Performance analysis of three-phase inverters controlled by synchronous delta-modulation systems," *IEEE Trans. Ind. Appl.*, vol. 30, no. 4, pp. 1016–1027, Aug. 1994.

[41] J.P. Vilain and C. Lesbroussart, "A new space vector modulation strategy for a three phase inverter: the space vector based delta-sigma modulation," *Journal de Physique III*, vol. 5, no. 7, pp. 1075–1088, July 1995.

[42] G. Venkataramanan, *Topology, Analysis and control of a Resonant dc link power converter*, Ph.D. dissertation, University of Wisconsin-Madison, 1992.

[43] J. Paramesh and A. von Jouanne, "Use of sigma-delta modulation to control emi from switch-mode power supplies," *IEEE Trans. on Industrial Electronics*, pp. 1365–1372, Feb. 2001.

[44] A. Mertens and H. Skudelny, "Calculations on the spectral performance of discrete pulse modulation strategies," in *Proc. Power Electronics Specialists Conf.*, Boston, June 1991, pp. 357–365.

[45] J.E. Iwersen, "Calculated quantizing noise of single-integration delta-modulation coders," *Bell Syst. Tech. J.*, pp. 2359–2389, 1969.

[46] J. Niezńanski, "Performance characterization of vector sigma-delta modulation," in *Proc. Ind. Elect. Soc.*, 1998, vol. 1, pp. 531–536.

[47] G. Luckjiff, I. Dobson, and D.M. Divan, "Modulator for resonant link converters," 1997, U.S. Patent No. 5,619,406.

[48] G. Luckjiff and I. Dobson, "Hexagonal sigma-delta modulation," *Submitted to IEEE Trans. Circuits Syst.*, 2003.

[49] H. Furstenberg, *Recurrence in Ergodic Theory and Combinational Number Theory*, Princeton Univ. Press, New Jersey, 1981.

[50] C. Corduneanu, *Almost Periodic Functions*, John Wiley & Sons, NY, 1968.

[51] Y. Katznelson, *An Introduction to Harmonic Analysis*, Dover, NY, second edition, 1976.

[52] W. Rudin, *Fourier Analysis on Groups*, Wiley, NY, 1962.

[53] R. Mãné, *Ergodic Theory and Differentiable Dynamics*, Springer-Verlag, NY, 1987.

[54] M. Spivak, *Calculus on Manifolds: A Modern Approach to Classical Theorems of Advanced Calculus*, Perseus Press, NY, 1965.

[55] K. Uchimura, T. Hayashi, T. Kimura, and A. Iwata, "VLSI A to D and D to A converters with multi-stage noise shaping modulators," in *Proc. ICASSP*, Tokyo, 1986, pp. 1545–1548.

[56] Y. Matsuya, K. Uchimura, A. Iwata, T. Kobayashi, and M. Ishikawa, "A 16*b* oversampling conversion technology using triple integration noise shaping," in *Proc. IEEE Int. Solid State Circuits Conf.*, Feb. 1987, pp. 48–49.

[57] S.K. Tewksbury and R.W. Hallock, "Oversampled, linear predictive and noise-shaping coders of order $n > 1$," *IEEE Trans. Circuits Syst.*, vol. 25, pp. 436–447, July 1978.

[58] D.J. Goodman and L.J. Greenstein, "Quantizing noise of dm/pcm encoders," *Bell Syst. Tech. J.*, vol. 52, pp. 183–204, Feb. 1973.

[59] D.B. Ribner, "A comparison of modulator networks for high-order oversampled ΣΔ analog-to-digital converters," *IEEE Trans. Circuits Syst.*, vol. 40, no. 8, pp. 461–466, Aug. 1993.

[60] A.M. Thurton, T.H. Peace, and M.J. Hawksford, "Bandpass implementation of the sigma delta A/D conversion technique," in *Proc. IEE Int. Conf. on (A/D) and (D/A) Conversion*, Swansea, U.K., Sept. 1991, pp. 81–85.

[61] O. Shoaei and W.M. Snelgrove, "Optimal (bandpass) continuous time ΣΔ modulator," in *Proc. ISCAS*, London, May 1994, pp. 489–492.

[62] L.H. Koopmans, *The Spectral Analysis of Time Series*, Academic Press, San Diego, 1974.

[63] J. Niezńanski, "Pulse density modulation for power electronics," Elektryka 567, Polytechnica Gedanensis, Gdańsk, 1998.

[64] R. Schreier, "The delta-sigma toolbox," 1998, MATLAB.

[65] T. Ritoniemi, T. Karema, and H. Tenhunen, "Design of stable high order 1-bit sigma delta modulators," in *Proc. ISCAS*, New Orleans, May 1990, pp. 3267–3270.

[66] C. Kok and T. Chen, "Vector valued sigma delta modulators for color image applications," in *Proc. Int. Conf. on Image Processing*, Santa Barbara, Oct. 1999, pp. 22–24.

[67] R.W. Adams, "Design and implementation of an audio 18-bit analog to digital converter using oversampling techniques," *J. Audio Eng. Soc.*, vol. 34, no. 3, pp. 153–166, Mar. 1986.

[68] A. Zygmund, *Trigonometric Series*, Cambridge Univ. Press, second edition, 1959.

Appendix A: Fourier and Ergodic Results on H

We transform standard Fourier and ergodic results from the square $[0,1)^2$ to H. Relate coordinates x' on $[0,1)^2$ to coordinates x on H by

$$x' = \langle Vx \rangle$$
$$x = \overline{\langle Wx' \rangle}$$

Relate coordinates p on Λ^* to coordinates p' on $\mathbb{Z}^{*2}$ by

$$p' = pW$$

Suppose $f' \in L^2([0,1)^2)$ and let $f = f' \circ \langle\,\rangle \circ V \in L^2(H)$. Then

$$f'(x') = f'(\langle Vx \rangle) = f(x)$$
$$dx = |H| dx'$$
$$\langle p'x' \rangle = \langle pW \langle Vx \rangle \rangle = \langle px \rangle$$

Write

$$(f,g) = \frac{1}{|H|} \int_H f(x) g^*(x) dx$$
$$(f',g') = \int_{[0,1)^2} f'(x') g'^*(x') dx'$$

Then

$$(f,g) = (f',g')$$
$$\hat{f}_p = (f, e^{-i2\pi px}) = (f', e^{-i2\pi p'x'}) = \hat{f}'_{p'}$$

Moreover,

$$f(\ \overline{\langle x+y \rangle}\ ) = f'(\langle V\ \overline{\langle x+y \rangle}\ \rangle) = f'(\langle V(x+y) \rangle) = f'(\langle x'+y' \rangle)$$

Hence the following results can be transformed to the results of section 4.4:

Fourier analysis on $[0,1)^2$ [68]: $L^2([0,1)^2)$ is a Hilbert space with inner product (f', g'). $\{e^{i2\pi p'x'} \mid p' \in \mathbb{Z}^{*2}\}$ is a complete orthonormal basis.

$$f'(x') = \sum_{p' \in \mathbb{Z}^{*2}} \hat{f}'_{p'} e^{i2\pi p'x'}$$

where the equality is interpreted in the L^2 sense and

$$\hat{f}'_{p'} = (f', e^{-i2\pi p'x'})$$

The Parseval formula is

$$(f', g') = \sum_{p' \in \mathbb{Z}^{*2}} \hat{f}'_{p'} \hat{g}'^{*}_{p'}$$

Manẽ [53] (Theorem II 3.2, Proposition II 2.7, Theorem I 9.2) implies: Let $\beta' \in \mathbb{R}^2$ be such that the only $p' \in \mathbb{Z}^{*2}$ with $p'\beta' \in \mathbb{Z}$ is $p' = 0$. Let $\tilde{f}' : \mathbb{R}^2/\mathbb{Z}^2 \to \mathbb{R}$ be continuous. Let π be the canonical projection $\mathbb{R}^2 \to \mathbb{R}^2/\mathbb{Z}^2$. Then translation by $\pi\beta'$ is a uniquely ergodic shift on $\mathbb{R}^2/\mathbb{Z}^2$ and, for all $e'_0 \in \mathbb{R}^2$,

$$\lim_{L\to\infty} \frac{1}{L} \sum_{n=0}^{L-1} \tilde{f}'(\pi \langle e'_0 + n\beta' \rangle) = \int_{\mathbb{R}^2/\mathbb{Z}^2} \tilde{f}'(s')ds'$$

(Note that $\pi(e'_0 + n\beta') = \pi \langle e'_0 + n\beta' \rangle$.) Suppose that $f' : [0,1)^2 \to \mathbb{R}$ lifts to $\tilde{f}'$ so that $f' = \tilde{f}' \circ \pi$. Then

$$\lim_{L\to\infty} \frac{1}{L} \sum_{n=0}^{L-1} f'(\langle e'_0 + n\beta' \rangle) = \int_{[0,1)^2} f'(s')ds'$$

Appendix B: Three Cases for β

We prove that there are three cases for $\beta \in H$ and characterize them.

Case 1 is $\{s \in \Lambda^* \mid s\beta \in \mathbb{Z}\} = \{0\}$. Suppose that Case 1 does not hold; that is, there is $r \in \Lambda^*$, $r \neq 0$ with $r\beta = z \in \mathbb{Z}$. We describe the general form of such a β. Suppose that $r = (r_1, r_2)V$ where $(r_1, r_2) \in \mathbb{Z}^{*2}$ and let g be the greatest common divisor of r_1, r_2. By dividing r and z by any common factors of z and g, we may assume that z and g are relatively prime. Also $r_1/g, r_2/g$ are relatively prime and by Euclid's algorithm there is $(\sigma_1, \sigma_2)^t \in \mathbb{Z}^2$ with $\frac{r_1}{g}\sigma_1 + \frac{r_2}{g}\sigma_2 = 1$. Let $\sigma = W(\sigma_1, \sigma_2)^t \in \Lambda$. Then $r\sigma = g$ and $x = (z/g)\sigma$ is a particular solution to the equation $rx = z$. The general solution to $rx = z$ is $x = \alpha r_\perp + (z/g)\sigma$ where $r_\perp = W(-r_2, r_1)^t \in \Lambda$ and $\alpha \in \mathbb{R}$. Therefore

$$\beta = \alpha r_\perp + \frac{z}{g}\sigma \tag{B.1}$$

for some $\alpha \in \mathbb{R}$. Case 2 is α irrational and Case 3 is α rational.

First we further characterize the β in Case 2 as satisfying

$$\{s \in \Lambda^* \mid s\beta \in \mathbb{Z}\} = \{mr \mid m \in \mathbb{Z}\} \tag{B.2}$$

It is clear that $\{s \in \Lambda^* \mid s\beta \in \mathbb{Z}\} \supset \{mr \mid m \in \mathbb{Z}\}$. To prove $\{s \in \Lambda^* \mid s\beta \in \mathbb{Z}\} \subset \{mr \mid m \in \mathbb{Z}\}$, suppose that $s\beta = \alpha s r_\perp + (z/g)s\sigma = z' \in \mathbb{Z}$ for $s \in \Lambda^*$. Then, since $s\sigma \in \mathbb{Z}$, $\alpha s r_\perp$ must be rational and it follows from α irrational that

$$0 = s r_\perp = (s_1, s_2)VW \begin{pmatrix} -r_2 \\ r_1 \end{pmatrix} = r_1 s_2 - r_2 s_1$$

Now

$$gs = \begin{pmatrix} s_1(r_1\sigma_1 + r_2\sigma_2) \\ s_2(r_1\sigma_1 + r_2\sigma_2) \end{pmatrix} = \begin{pmatrix} s_1 r_1\sigma_1 + s_2 r_1\sigma_2 \\ s_1 r_2\sigma_1 + s_2 r_2\sigma_2 \end{pmatrix} = s\sigma\, r \tag{B.3}$$

and $gz' = gs\beta = (s\sigma)r(z/g)\sigma = (s\sigma)z$. But g and z are relatively prime, so that g divides $s\sigma$ and (B.3) implies that $(s\sigma)/g = m$ is an integer such that $s = mr$.

Now we use (B.2) to prove in Case 2 that for $s \in \Lambda^*$,

$$s\beta \in \mathbb{Z} \iff \left\{ \begin{array}{l} sr_\perp = 0 \\ s\sigma = 0 \pmod{g} \end{array} \right\} \tag{B.4}$$

Suppose that $s\beta \in \mathbb{Z}$. Then (B.2) implies that $s = mr$ for $m \in \mathbb{Z}$ and hence that $sr_\perp = 0$. Moreover $s\beta = s((z/g)\sigma) = (z/g)s\sigma \in \mathbb{Z}$ and since g and z are relatively prime, g divides $s\sigma$ and $s\sigma = 0 \pmod{g}$. The implication $\Leftarrow$ in (B.4) follows directly from (B.1).

In Case 3, $\beta = \alpha r_\perp + (z/g)\sigma$ with α rational. Then β has the form $\beta = (h/q)v$ for $v = W(v_1, v_2)^t \in \Lambda$, where h and q are integers. Without loss of generality we can assume that h and q are relatively prime and that v_1 and v_2 are relatively prime. By Euclid's algorithm there is $(\rho_1, \rho_2) \in \mathbb{Z}^{*2}$ with $\rho_1 v_1 + \rho_2 v_2 = 1$. Let $\rho = (\rho_1, \rho_2)V \in \Lambda^*$. Also let $v_\perp = (-v_2, v_1)V \in \Lambda^*$.

We further characterize the β in Case 3 as satisfying $\{s \in \Lambda^* \mid s\beta \in \mathbb{Z}\} = \{z_1 v_\perp + z_2 q\rho \mid z_1, z_2 \in \mathbb{Z}\}$. It is clear that $\{s \in \Lambda^* \mid s\beta \in \mathbb{Z}\} \supset \{z_1 v_\perp + z_2 q\rho \mid z_1, z_2 \in \mathbb{Z}\}$. To prove $\{s \in \Lambda^* \mid s\beta \in \mathbb{Z}\} \subset \{z_1 v_\perp + z_2 q\rho \mid z_1, z_2 \in \mathbb{Z}\}$, suppose that $s\beta = \frac{h}{q} sv = z \in \mathbb{Z}$ with $s \in \Lambda^*$. Then $hsv = qz$ and h and q relatively prime imply that h divides z and $z_2 = z/h$ is an integer. Then $x = q(z/h)\rho = z_2 q\rho$ is a particular solution to the equation $x\beta = z$ with $x \in \Lambda^*$. The general solution to $x\beta = z$ is $x = z_1 v_\perp + z_2 q\rho$, $z_1 \in \mathbb{R}$. Since we require $x \in \Lambda^*$, $z_1 v_\perp = x - z_2 q\rho \in \Lambda^*$, and, since v_1 and v_2 are relatively prime, z_1 is an integer.

Appendix C: Fourier Coefficients for ⬡

We derive (4.21) for the Fourier coefficients of the hexagon part operator ⬡ . Equation (4.20) implies $c_0 = 0$. Now we compute c_p for $p \neq 0$. Define $a : \mathcal{P}^* \to \mathbb{R}$ by $a(p) = -\int_H e^{-i2\pi px} dx$. Then

$$c_p = \frac{1}{|H|} \int_H \langle s \rangle \, e^{-i2\pi ps} ds = \frac{1}{i2\pi |H|} (D_p a(p))^t \tag{C.1}$$

and the calculation reduces to finding an expression for $a(p)$:

$$\begin{aligned} a(p) &= \frac{p}{i2\pi pp^t} \int_H (D_x e^{-i2\pi px})^t dx \\ &= \frac{p}{i2\pi |p|^2 |n^\perp|} \oint_{\partial H} e^{-i2\pi p\ell} n_\ell^\perp d\ell \\ &= \frac{|n|}{i2\pi |p|^2 |n^\perp|} \sum_{s \in \pm\{a,b,c\}} p n_s^\perp \int_{-\frac{1}{2}}^{\frac{1}{2}} e^{-i2\pi p \sigma_s(t)} dt \end{aligned}$$

where $\sigma_s(t) = \frac{1}{2} n_s^\perp + n_s t$, $t \in [-1/2, 1/2]$ parameterizes the hexagon edges. Then letting $p_s = pn_s$ and $p_s^\perp = pn_s^\perp$ gives

$$\begin{aligned} a(p) &= \frac{-|n|}{\pi |n^\perp| |p|^2} \sum_{s \in \{a,b,c\}} p_s^\perp \int_{-\frac{1}{2}}^{\frac{1}{2}} \sin(2\pi p \sigma_s(t)) dt \\ &= \frac{-1}{\pi^2 \sqrt{3} |p|^2} \sum_{s \in \{a,b,c\}} \frac{p_s^\perp}{p_s} \sin(\pi p_s) \sin(\pi p_s^\perp) \end{aligned} \tag{C.2}$$

Substituting (C.2) in (C.1), differentiating, and evaluating at $p \in \Lambda^*$ (then $p_s^\perp \in \mathbb{Z}$ and $\sin(\pi p_s^\perp) = 0$) yields

$$c_p = \frac{i}{6\pi^2 |p|^2} \sum_{s \in \{a,b,c\}} \frac{p_s^\perp}{p_s} \sin(\pi p_s) \cos(\pi p_s^\perp) n_s^\perp \tag{C.3}$$

In the case $p \in \Lambda^t - \{0\}$, $p_s \in \mathbb{Z}$ and $\sin(\pi p_s)/(\pi p_s) = 0$ and $c_p = 0$ except when $p_s = 0$. When $p_s = 0$, $p = k n_s^{\perp t}$, $k \in \mathbb{Z}$, $p_s^\perp = 2k$ and (4.21) with $p \in \Lambda^t - \{0\}$ follows from (C.3).

To simplify (C.3) in the case $p \in \Lambda^* - \Lambda^t$, consider $f_s : \Lambda^* \to \mathbb{R}$ defined by

$$f_s(p) = 2 \sin(\pi p_s) \cos(\pi p_s^\perp) = \sin(\pi p n_s^+) + \sin(\pi p n_s^-)$$

where $n_s^{\pm} = n_s \pm n_s^{\perp}$. Notice that $n_s^{\pm} \in 2\Lambda^{*t}$. Let $\lambda \in \Lambda$. Then

$$f_s(p+\lambda^t) = \sin(\pi(p+\lambda^t)n_s^+) + \sin(\pi(p+\lambda^t)n_s^-) = f_s(p)$$

since $n_s^{\pm} \in 2\Lambda^{*t}$ implies that $\lambda^t n_s^{\pm}$ is an *even* integer. This periodicity of f_s implies that f_s is constant on each of $n_a^t + \Lambda^t$ and $-n_a^t + \Lambda^t$. The respective constants can be directly calculated: $f_s(\pm n_a^t) = \pm\sqrt{3}$ for $s = a, b, c$. Then $f_s(p) = \operatorname{sgn}(p)\sqrt{3}$ and

$$\begin{aligned} c_p =& \frac{i \operatorname{sgn}(p)}{4\sqrt{3}\pi^2|p|^2} \sum_{s\in\{a,b,c\}} \frac{p_s^{\perp}}{p_s} n_s^{\perp} \\ =& \frac{i \operatorname{sgn}(p)}{4\sqrt{3}\pi^2|p|^2} \begin{bmatrix} \frac{p_a-p_c}{p_b} + \frac{p_a-p_b}{p_c} \\ \frac{p_b-p_c}{p_a} + \frac{p_b-p_a}{p_c} \\ \frac{p_c-p_b}{p_a} + \frac{p_c-p_a}{p_b} \end{bmatrix}, \qquad p \in \Lambda^* - \Lambda^t. \end{aligned}$$

Using $p_a + p_b + p_c = 0$ we obtain (4.21) for $p \in \Lambda^* - \Lambda^t$.

Appendix D: Absolute Summability

We prove that the coefficents $\sum_{p\in\Lambda^*} |[c_p \otimes c_p^*]_{i,j}| < \infty$ for each matrix element indexed by i, j.

For the case $p \in \{(n_a^t + \Lambda^t) \cup (-n_a^t + \Lambda^t)\}$, $c_p \sim \frac{p^t}{\Pi(p)}$. Using $p = \pm n_a^t + (n_1, n_2)W^t$ where $(n_1, n_2) \in \mathbb{Z}^2$ we have

$$\sum_{p\in\{(n_a^t+\Lambda^t)\cup(-n_a^t+\Lambda^t)\}} |[c_p \otimes c_p^*]_{i,j}| \sim \sum_{(n_1,n_2)\in\mathbb{Z}^2} \frac{1}{n_1^2 n_2^2} < \infty$$

For the case $p \in \{\Lambda^t | p_a p_b p_c = 0, p \neq 0\}$, the sum is over points in three lines and $c_p \sim \left(\frac{p_a}{p_b p_c}, \frac{p_b}{p_a p_c}, \frac{p_c}{p_a p_b}\right)^t$. Using $p = (n_1, n_2)W^t$ where $(n_1, n_2) \in \mathbb{Z}^2$ we have

$$\sum_{p\in\{\Lambda^t | p_a p_b p_c = 0, p\neq 0\}} |[c_p \otimes c_p^*]_{i,j}| \sim \sum_{n\in\mathbb{Z}} \frac{1}{n^2} < \infty$$